JGR Solid Earth

RESEARCH ARTICLE
10.1029/2019JB018001

# Structural Control on Megathrust Rupture and Slip Behavior: Insights From the 2016 Mw 7.8 Pedernales Ecuador Earthquake

**Lillian Soto-Cordero[1], Anne Meltzer[1], Eric Bergman[2], Mariah Hoskins[1], Joshua C. Stachnik[1], Hans Agurto-Detzel[3], Alexandra Alvarado[4], Susan Beck[5], Philippe Charvis[3], Yvonne Font[3], Gavin P. Hayes[6], Stephen Hernandez[4], Colton Lynner[5,7], Sergio Leon-Rios[8], Jean-Mathieu Nocquet[3], Marc Regnier[3], Andreas Rietbrock[8], Frederique Rolandone[9], and Mario Ruiz[4]**

[1]Department of Earth and Environmental Sciences, Lehigh University, Bethlehem, PA, USA, [2]Global Seismological Services, Golden, CO, USA, [3]Université Côte d'Azur IRD, Géoazur, IRD, Nice, France, [4]Instituto Geofísico at the Escuela Politécnica Nacional, Quito, Ecuador, [5]Department of Geosciences, University of Arizona, Tucson, AZ, USA, [6]National Earthquake Information Center, U.S. Geological Survey, Golden, CO, USA, [7]Now at Department of Earth Sciences, University of Delaware, Newark, DE, USA, [8]Geophysical Institute, Karlsruhe Institute of Technology, Karlsruhe, Germany, [9]Sorbonne Université, CNRS-INSU, Institut des Sciences de la Terre Paris, Paris, France

**Key Points:**
- A dense temporary seismic network provides a detailed view of the evolution of a megathrust rupture postseismic sequence
- The postseismic sequence is characterized by clusters of seismicity containing earthquake swarms and moderate to large aftershocks
- Seafloor topography and upper plate structure segment the subduction zone and control slip behavior across the seismic cycle

**Supporting Information:**
- Supporting Information S1

**Correspondence to:**
A. Meltzer,
ameltzer@lehigh.edu

**Citation:**
Soto-Cordero, L., Meltzer, A., Bergman, E., Hoskins, M., Stachnik, J. C., Agurto-Detzel, H., et al. (2020). Structural control on megathrust rupture and slip behavior: Insights from the 2016 Mw 7.8 Pedernales Ecuador earthquake. *Journal of Geophysical Research: Solid Earth*, *125*, e2019JB018001. https://doi.org/10.1029/2019JB018001

Received 8 MAY 2019
Accepted 17 JAN 2020
Accepted article online 17 FEB 2020



**Abstract** The heterogeneous seafloor topography of the Nazca Plate as it enters the Ecuador subduction zone provides an opportunity to document the influence of seafloor roughness on slip behavior and megathrust rupture. The 2016 $M_w$ 7.8 Pedernales Ecuador earthquake was followed by a rich and active postseismic sequence. An internationally coordinated rapid response effort installed a temporary seismic network to densify coastal stations of the permanent Ecuadorian national seismic network. A combination of 82 onshore short and intermediate period and broadband seismic stations and six ocean bottom seismometers recorded the postseismic Pedernales sequence for over a year after the mainshock. A robust earthquake catalog combined with calibrated relocations for a subset of magnitude ≥4 earthquakes shows pronounced spatial and temporal clustering. A range of slip behavior accommodates postseismic deformation including earthquakes, slow slip events, and earthquake swarms. Models of plate coupling and the consistency of earthquake clustering and slip behavior through multiple seismic cycles reveal a segmented subduction zone primarily controlled by subducted seafloor topography, accreted terranes, and inherited structure. The 2016 Pedernales mainshock triggered moderate to strong earthquakes ($5 \leq M \leq 7$) and earthquake swarms north of the mainshock rupture close to the epicenter of the 1906 $M_w$ 8.8 earthquake and in the segment of the subduction zone that ruptured in 1958 in a $M_w$ 7.7 earthquake.

## 1. Introduction

Subduction zones produce the largest earthquakes on Earth, releasing significant amounts of stored energy. As a result, megathrust earthquakes, and associated ground shaking, tsunamis, and landslides, can result in significant socio-economic impacts and loss of life (e.g., Mw 9.5 Chile 1960, Mw 9.2 Alaska 1964, Mw 9.1 Sumatra 2004, and Mw 9.0 Tohoku 2011). A better understanding of the processes governing megathrust rupture is critical to assess their seismic and tsunami potential and hazards. Advances in geophysical monitoring and research during the past decades show that subduction zones exhibit diverse modes of slip behavior. Variable slip velocities and duration range from stick-slip earthquakes, slow slip events (SSEs), to aseismic creep (e.g., see reviews by Peng & Gomberg, 2010; Bilek & Lay, 2018, and references therein). These observations reveal heterogenous frictional properties downdip and along-strike on the plate interface due to lateral variations in structure or mechanical properties. Roughness on the downgoing plate (e.g., seamounts, seafloor offsets, and ridges) and sediment thickness in the trench can act as asperities or as barriers inhibiting rupture segmenting the subduction zone (Bangs et al., 2006; Husen et al., 2002; Kodaira et al., 2000; Wang & Bilek, 2011; Wang & Bilek, 2014). Structure within the overriding plate, accreted terranes, forearc basins, and faults can also influence rupture behavior (e.g., Basset et al., 2016; Hicks et al., 2014). Slow-slip events as well as earthquakes in the downgoing slab and overriding plate can be triggered by megathrust events (Gomberg & Sherrod, 2014).

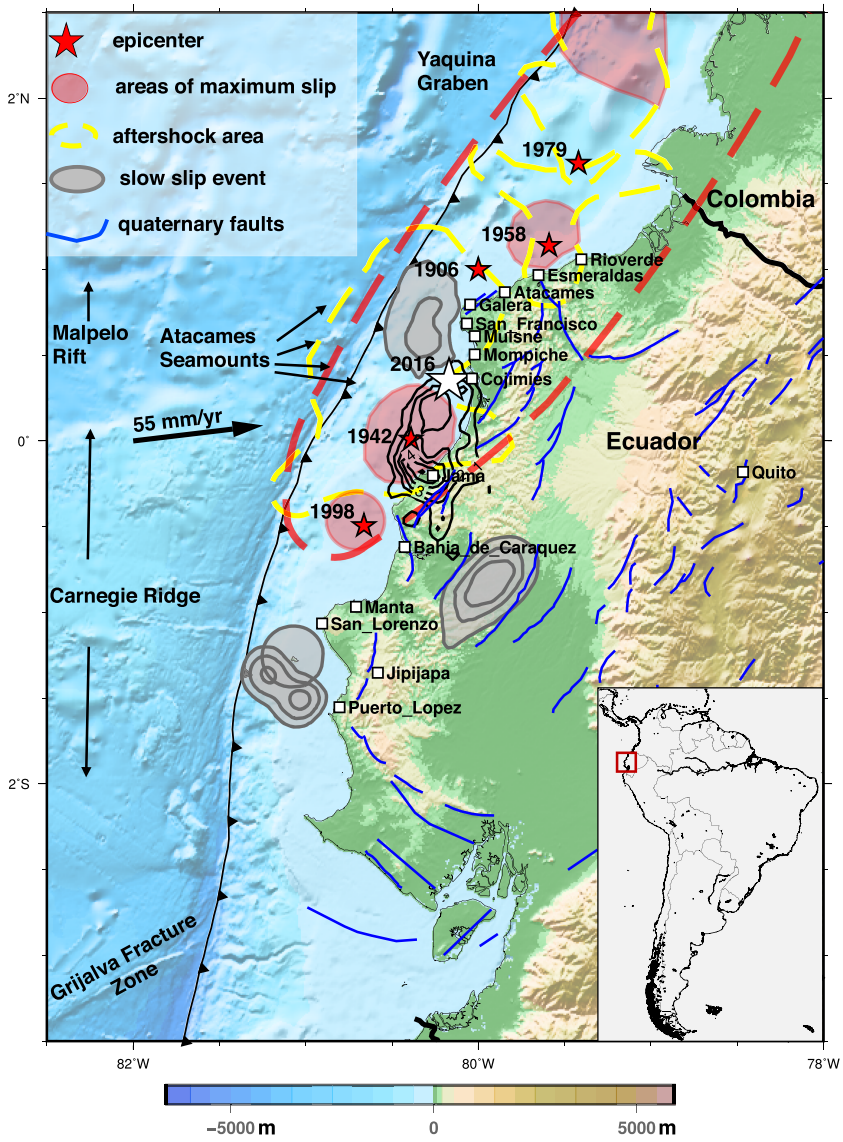


**Figure 1.** Map of Ecuador subduction zone. Inset South America, Ecuador outlined by red box. The black contours and white star show the 16 April 2016 $M_w$ 7.8 Pedernales earthquake rupture and mainshock epicentral location (Nocquet et al., 2017). Coseismic slip contours 1 m, maximum slip 6 m. The red stars indicate the epicentral locations of large historic earthquakes; the red shaded regions indicate the areas of major moment release (Beck & Ruff, 1984; Kanamori & McNally, 1982; Swenson & Beck, 1996; Yepes et al., 2016); the dashed yellow contours indicate the aftershock areas (Mendoza & Dewey, 1984); the red dashed line indicates the partial rupture area the 1906 earthquake (Collot et al., 2004). The continuous gray contours (5-cm interval) regions of slow slip events (Rolandone et al., 2018; Vaca et al., 2018; Vallée et al., 2013). The large black arrow indicates the Nazca-South America relative motion (Kendrick et al., 2003). The blue lines indicate the Quaternary faults (Eguez et al., 2003). Major bathymetric features including the Carnegie Ridge and Atacames Seamounts are identified along the subducting Nazca Plate. Coastal towns mentioned in the text labeled.

In April 2016, the Mw 7.8 Pedernales, Ecuador, earthquake ruptured an approximately 100-km × 40-km segment of the subduction zone east and northeast of the intersection of the Carnegie ridge with the trench (Figure 1). In the wake of the mainshock, an international rapid response effort coordinated by the Instituto Geofísico at the Escuela Politécnica Nacional (IGEPN) in Quito deployed a temporary network of seismometers along the North Ecuador subduction zone (Meltzer et al., 2019). These temporary stations densified coastal stations of the permanent national network (RENSIG; Alvarado et al., 2018). Automatically detecting and locating earthquakes is an integral part of earthquake monitoring and postevent data analysis. Detecting, associating, and locating aftershocks from a large magnitude earthquake is particularly

challenging. The increased rate of seismicity following the mainshock and the potential for overlapping events (where the onset of a new event overlaps with the coda of a previous event) makes it difficult to accurately capture the complete postseismic sequence. Rapid response efforts like the Pedernales deployment present additional challenges given the range of frequency responses associated with the diverse suite of instruments. Nevertheless, a robust earthquake catalog is essential to studying earthquake sequences. The spatio-temporal evolution of earthquake sequences provides insight into earthquake rupture and postseismic deformation and if monitored in near-real time can contribute to aftershock forecasting and hazard analysis in the weeks and months after large earthquakes.

In this study we present analysis of the 2016 Pedernales earthquake and seismic activity following the event integrating an earthquake catalog generated through an automatic processing scheme with calibrated earthquake locations. We relocate the mainshock, foreshock, and aftershocks greater than Ml 4 using the hypocentroidal decomposition method (HDC). We describe and make available the earthquake catalog. We explore in detail the spatial and temporal evolution of the seismic sequence following the mainshock and place the sequence in the context of past ruptures of large earthquakes, SSEs, and background seismicity along the Ecuador subduction margin. Our results document the persistence of spatially focused seismicity over multiple seismic cycles, the role of seafloor topography and upper plate structure as controls on seismicity, and the interplay between slow slip and earthquakes in the earthquake cycle.

## 2. The North Ecuador Subduction Margin and the Pedernales Rupture

The Ecuador subduction zone accommodates convergence between the Nazca and South America Plates. Plate coupling along the margin varies significantly along strike (Chlieh et al., 2014; Marcaillou et al., 2016; Nocquet et al., 2014; Rolandone et al., 2018). The subducting Nazca Plate exhibits pronounced seafloor topography, with seamounts, ridges, rifts, and faults intersecting the trench (Figure 1). The Carnegie Ridge, an ~200 km wide, 1.5- to 2-km high oceanic plateau formed as a result of the eastward movement of the Nazca Plate over the Galapagos hotspot, subducts beneath the margin (Graindorge et al., 2004; Gutscher et al., 1999; Lonsdale, 1978). The north-south Atacames Seamount chain sits north of the Carnegie Ridge and is also subducting beneath the margin (Collot et al., 2005; Marcaillou et al., 2016). The subduction of bathymetric features affects interplate coupling (Wang & Bilek, 2014). Some studies consider seamounts as strong asperities, enhancing coupling at the interface and promoting earthquake nucleation (Cloos, 1992; Scholz & Small, 1997). Other studies argue that the subduction of seafloor topography acts as a barrier slowing or preventing earthquake rupture propagation (Das & Watts, 2009; Wang & Bilek, 2011).

The forearc is exposed on land and is composed of a series of Mesozoic accreted oceanic terranes and Cenozoic sedimentary basins (Jaillard et al., 2000; Jaillard et al., 2009; Marcaillou & Collot, 2008; Reynaud et al., 1999). The forearc and parts of the arc sit within the North Andean Sliver, a block of material between the trench and the South American craton (Alvarado et al., 2016; Nocquet et al., 2014; White et al., 2003). Abundant faults, inherited from terrane accretion and more recent Cenozoic deformation, occur in the forearc (Figure 1; Reyes & Michaud, 2012; Eguez et al., 2003).

The subduction zone offshore Northern Ecuador exhibits a range of seismic and aseismic slip behavior including large megathrust earthquakes, SSEs, earthquake swarms, repeating earthquakes, and aseismic creep. In 1906 an ~500-km-long segment of the subduction zone ruptured offshore northern Ecuador and Colombia in a Mw 8.8 earthquake (Figure 1; Kelleher, 1972; Abe, 1979; Swenson & Beck, 1996). The 1906 rupture stopped at the intersection of the Carnegie Ridge with the trench. Three large historic earthquakes ruptured different sections of the 1906 rupture area: from south to north, the Mw 7.8 1942, Mw 7.7 1958, and Mw 8.2 1979 earthquakes (Figure 1; Beck & Ruff, 1984; Kanamori & McNally, 1982; Mendoza & Dewey, 1984; Swenson & Beck, 1996). Recent analysis of tsunami records from the 1906 earthquake indicate large slip near the trench suggesting that perhaps the source region for the 1906 event does not coincide with these more recent large events (Yoshimoto et al., 2017). Models of interseismic plate coupling derived from Global Positioning System (GPS) data show that the epicenters of the 1942, 1958, and 1979 earthquakes locate within or at the border of locked asperities (Chlieh et al., 2014). These data suggest a 50-km-long creeping segment south of the axis of the Carnegie Ridge that appears to have acted as a barrier, preventing rupture propagation of the 1906 and 1942 earthquakes to the south. Analyses of geodetic signals from a continuous GPS network, and investigation of seismic swarms and repeating earthquakes, have identified regions of

episodic and temporally discrete SSEs offshore the Punta Galera-Mompiche region and offshore Manta-La Plata Island (Figure 1; Holtkamp et al., 2011; Mothes et al., 2013; Vallée et al., 2013; Chlieh et al., 2014; Rolandone et al., 2018; Vaca et al., 2018; Segovia et al., 2018). These events last from days to weeks and up to several months and have equivalent moment magnitudes ranging from 6.0 up to 7.1 (Rolandone et al., 2018; Vaca et al., 2018; Vallée et al., 2013). Consequently, aseismic slip along the margin contributes significant moment release as part of the earthquake cycle.

The April 2016, Mw 7.8 Pedernale mainshock was preceded by a Mw 4.8 foreshock 11 min earlier. The mainshock rupture initiated in and propagated through a region of moderate to high interseismic coupling (Chlieh et al., 2014; Nocquet et al., 2017). Fault slip models for the 2016 earthquake show that the rupture broke through two discrete asperities, initiating in the northern asperity and propagating south (National Earthquake Information Center (NEIC), 2016c; Ye et al., 2016; Nocquet et al., 2017; Yi et al., 2018). Two slip patches, one in the north with ~3 m of slip and one in the south with 5–6 m of slip, are connected by a region of lower slip (~1–2 m) in the central portion of the rupture. The location of the mainshock and slip derived from teleseismic data (NEIC, 2016c) combined with either tsunami data (Ye et al., 2016) or InSAR (Yi et al., 2018) locate the mainshock on land near the coast with maximum slip close to the coast in the north and beneath the coastline to the south. Incorporating data from local GPS and accelerometers with InSAR and teleseismic data shift the mainshock and northern patch of slip offshore, 30 km to the west (Nocquet et al., 2017). The source time function, ground motion records, shaking intensity, and damage reports are consistent with southward directivity of the rupture and maximum slip beneath the coast to the south. Immediately after the mainshock, two patches of afterslip, each covering an area approximately 50 km × 50 km, were observed updip to the north and south of the mainshock rupture (Rolandone et al., 2018). Over a 30-day period, the northern slip patch released an equivalent moment magnitude of Mw 7.1 and the southern patch released an equivalent moment magnitude of Mw 7.0 (Rolandone et al., 2018). A third patch of afterslip was observed at approximately 50-km depth downdip of the mainshock rupture with an equivalent moment magnitude of Mw 6.7 to 6.8 (Rolandone et al., 2018). Approximately a week after the mainshock, a triggered SSE initiated near the trench, approximately 100 km south of the mainshock rupture (Rolandone et al., 2018). This SSE had an equivalent moment magnitude of Mw 6.7 to 6.8

Comparison of seismic waveforms, source time functions, and magnitudes suggest that the rupture area of the 2016 Pedernales earthquake overlaps with both the Mw 7.8 1942 rupture and the southern portion of the Mw 8.8 1906 rupture (Nocquet et al., 2017; Ye et al., 2016). Nocquet et al. (2017) suggest that megathrust rupture along the Ecuador-Colombian margin behaves as an earthquake supercycle, where great earthquakes are followed by clusters of large earthquakes on decadal time scales followed by long periods of quiescence.

## 3. Data and Methods

### 3.1. Data

A dense network of broadband, intermediate, and short-period seismometers were installed between 9 and 22 May 2016, beginning 23 days after the mainshock (Figure S1 in the supporting information; Meltzer et al., 2019). These stations were in place for a year (into May 2017), with a small number of stations remaining in the field into July 2017. Short-period three-component ocean bottom seismometers (OBS) were installed at the end of May 2016 and recorded 5.5 months of data into mid-November. The OBS stations provide azimuthal coverage of the postseismic sequence. Stations from the national network recorded postseismic events for the first 23 days after the mainshock prior to temporary network installation. From 28 May to 13 November 2016 (Julian day (JD) 2016:149–318) the largest number of stations recorded data simultaneously (for details of station recording see Figure S2). For this study we processed continuous data recorded by a total of 82 permanent and temporary stations located offshore and in the forearc region (Figure S1). We included data from permanent stations located only in the forearc to avoid structural complexities from stations in the arc. The mainshock occurred at 16 April 2016 23:58:36 UTC (JD 2016:107). The catalog starts immediately after the mainshock, 17 April 2016 00:00:00 (JD 2016:108) and extends through 4 July 2017 (JD 2017:185). We processed 240 channels of continuous time series data covering a period of 480 days.

### 3.2. Methods: Building the Pedernales Sequence Catalog

We tested three common detection algorithms that use characteristic functions of the time series to identify the onset of arrivals: (1) the traditional ratio of the short-term average and long-term average (STA/LTA) algorithm using predetermined windows and a single filter band (Allen, 1982), (2) a modification of the STA/LTA algorithm implementing a multiband filter processing scheme (Lomax et al., 2012), and (3) kurtosis as described by Baillard et al. (2014). We paired detections from these three methods with two different associators, the travel time grid associator in Antelope (dbgrassoc, BRTT Antelope Environmental Monitoring Software©) and the U.S. Geological Survey (USGS) global associator GLASS3 (Yeck et al., 2019). Both associators search over a precomputed travel time grid for a potential hypocenter that produces theoretical times that most closely correspond to the automatic picks obtained by the detectors. GLASS3 uses a Bayesian algorithm for event nucleation and association. To assess detector-associator pairs, we identified a set of manually reviewed control events and processed the continuous time series using various detector-associator combinations. We visually checked the automatic picks obtained by the detectors to assess their accuracy and evaluated the quality of the events obtained by each detector-associator pair. Soto-Cordero (2019) provides a detailed analysis and discussion of the tests performed. The traditional STA/LTA detector combined with the Antelope travel time grid associator produced the more robust automatic catalog. This combination was more effective in finding the largest number of confirmed earthquakes while producing the smallest number of false events (spurious signals associated as earthquakes) and minimizing the amount of split or multiple events (when the associator uses different combinations of picks to declare and locate an event yielding multiple locations for the same event).

We used BRTT Antelope Environmental Monitoring Software© to produce to an automatic catalog for the Pedernales sequence. Waveforms were band-pass filtered (P waves: 1-10 Hz, S waves: 1-5 Hz). Onset arrivals were detected using STA/LTA ratios on vertical and horizontal components for *P* and *S* waves respectively (*P* waves: STA: 2 s, LTA: 10 s; *S* waves: STA: 2 s, LTA: 15 s). Detections are associated into events and initial hypocenters determined using a precomputed travel time grid built with the iasp91 velocity model (Kennett & Engdahl, 1991). The 4° × 6° travel time grid was aligned with the orientation of the trench. The grid consisted of 151 grid nodes in each horizontal direction. A depth interval of 2 km was used in the upper 50 km followed by 5-km thick layers down to a depth of 170 km. A minimum of five phases were required for each event in the initial catalog. Initial locations are subsequently relocated by applying a generalized location scheme using Gauss-Newton minimization (e.g., genloc; Pavlis et al., 2004). Location errors are calculated by estimating location confidence ellipses. Traditional Richter (local) magnitude (Ml) is calculated automatically for events with signal to noise ratio >3.

### 3.3. Methods: Seismic Moment

To determine the seismic moment for moderate to large events, we performed a linear regression of 33 events in our catalog for which Mw was available (Figure S3) through the gCMT and National Earthquake Information Center (NEIC) databases to convert Ml to Mw. Using this relationship, we calculated moment magnitude for 86 events Ml ≥4.64 (the smallest magnitude event in our catalog for which Mw was available). For the four pairs of largest aftershocks, we retained the moment magnitude calculated by NEIC. The seismic moment was computed based on the moment magnitude equation, Mw=(log(m0)-16.1)/1.5 (Hanks & Kanamori, 1979). To assess the depth distribution of seismic moment of the Pedernales sequence, we computed the cumulative seismic moment in 5-km bins. To assess the spatial distribution of seismic moment, we generated a seismic moment density plot using the point density function within Esri ArcGIS Pro©.

### 3.4. Methods: Calibrated Relocations Using the HDC

We determined calibrated relocations for a subset of moderate to large earthquakes incorporating local, regional, and teleseismic phases using the HDC (Hayes et al., 2013; Jordan & Sverdrup, 1981; Karasözen et al., 2016;McNamara et al., 2014 ; Nealy et al., 2017). HDC is a multiple-event relocation technique that separates the relocation problem into two complementary steps: (1) relative location in space and time of individual events (cluster vectors) with respect to the position of the hypocentroid and (2) inversion for the absolute location of the hypocentroid. Since individual event locations are calculated with respect to an absolute location (the hypocentroid), each event is considered to have an absolute geographic calibrated location. Direct arrival phases, Pg and Sg, at short epicentral distances (<1.0°) are inverted for the location of

the hypocentroid. The use of phases at small epicentral distances results in short ray paths, thus diminishing travel-time errors from unknown velocity structure. All available phases at any epicentral distance (local, regional, and teleseismic) are inverted for the relocation of the cluster vectors. Cluster vectors are determined from travel-time differences to reduce cluster vector uncertainties and bias caused by unknown velocity heterogeneities (Karasözen et al., 2016).

A further advantage of the HDC method with respect to other relative location methods is that the location uncertainty is calibrated and estimated from the actual data. To calculate empirical reading errors, HDC gives priority to the consistency between repeated readings of the same phase-station pair for multiple events in a cluster instead of emphasizing the size of residuals against some reference travel time model. Empirical reading errors are estimated using a robust estimate of spread (Croux & Rousseeuw, 1992) of the travel-time residuals for each station-phase pair observed multiple times in the dataset. Empirical reading errors serve two functions: (1) to weight the arrival times in the inversion and (2) to identify outliers in the data. An iterative process for the detection and removal of outliers is followed: large thresholds are used initially to identify and remove outliers, and then HDC is run again to produce a new hypocentroid, new cluster vectors, and updated estimates of empirical reading errors. This process is repeated, while gradually lowering the threshold, until the spread of station-phase empirical reading errors reaches a normal distribution (McNamara et al., 2014; Nealy et al., 2017).

For the Pedernales sequence, we focused on events Ml $\geq$ 4.0 with focal depths shallower than 50 km. Regional and teleseismic phase arrivals from the International Seismological Centre catalog (Figure S4; International Seismological Centre, 2016) were integrated with near-source phases recorded by the permanent national network and temporary deployment stations (Figure S1). We selected events with good azimuthal coverage, OBS data, and depth phases. Earthquake locations with an azimuthal gap greater than 185° were excluded from the relocation process. Of 313 Ml $\geq$ 4.0 aftershocks, 87 earthquakes met the selection criteria. We manually reviewed these events, adding phases not detected in the automatic processing and adjusting picks as needed. Manual review and editing of this subset of events added 1,600 additional near-source/regional phases (mostly *S* picks; Figure S5). These events were relocated using the 1D iasp91 velocity model, and local magnitudes were recalculated prior to the HDC relocation process. We added the Ml 4.8 foreshock and Mw 7.8 mainshock to the HDC relocation. We also incorporated seven Mb 4.0–6.1 events from the interseismic coupling catalog that occurred from 1996 to 2015 (Table S1 in the supporting information). These events share readings from some of the same permanent stations that recorded the Pedernales sequence and their inclusion improved azimuthal coverage and depth constraints in the Manta region.

The velocity structure in subduction zones is inherently 3-D, and in Ecuador accreted forearc terranes impart strong north-south velocity heterogeneity in the crust (Font et al., 2013; Lynner et al., 2020). For the HDC inversion process, we separated the events into two clusters, a northern cluster extending from 1°N to −0.4°S and a southern cluster from −0.4 to −1.2°S. We then calculated a local 1-D velocity model for each cluster to avoid location bias due to velocity structure. The ak135 global model (Kennett et al., 1995) was used as an initial starting velocity model and modified iteratively to manually fit the phase arrival readings to the predicted travel time curves (Figure S6). A stable 1-D velocity structure was obtained from 21,907 phase readings from multiple events with fixed relative locations. Particular emphasis was given to constraining *P* wave and *S* wave velocities at near-source distances, $\leq$0.70° for the northern cluster and $\leq$0.50° for the southern cluster. The best fit is obtained with a two-layered crust over a half space (Figure S6). The azimuthal coverage at near-source distances for each cluster was very good, resulting in a stable hypocentroid with respect to changes in the local velocity structure.

During the relocation inversion, the latitude, longitude, depth, and origin time of each event can be set as a free or fixed parameter. The determination of focal depth and origin time usually carries the largest uncertainties and are dependent on the availability of arrival time data (preferably both *P* and *S*) from stations at short epicentral distance, the velocity model, and availability of depth phases from teleseismic arrivals (Karasözen et al., 2016). Although Pg and Sg phases up to distances of several times the focal depth provide good depth constraints for local events, for the Pedernales M>4 events, free-depth solutions were unstable. In this scenario, it is preferable to set depths manually by minimizing residuals at nearby stations while keeping the latitude, longitude, and origin time as free parameters. We performed fixed depth relocations

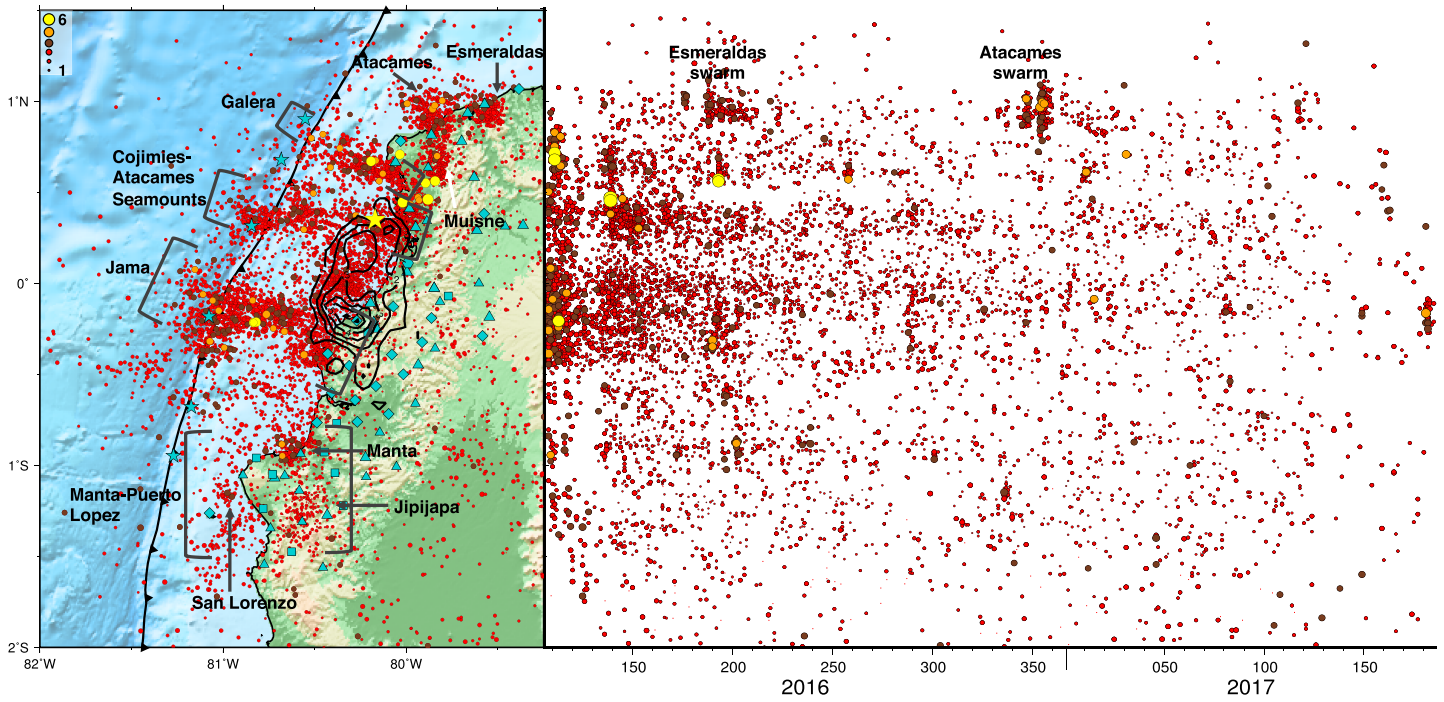


**Figure 2.** Distribution of seismic events contained in the Pedernales sequence automatic catalog 17 April 2016 (Julian day [JD] 2016:108) to 4 July 2017 (JD 2017:185), minimum of eight phases and hypocenter errors less than 10 km, $n$=9036 events. The left panel identifies earthquake composite clusters and swarms. The light blue symbols are stations used to generate the automatic catalog, triangles: broadband, diamonds: intermediate period, squares: short period, stars: OBS, hexagon: accelerometer (see Figures S1 and S2 in the electronic supplement for additional details). The right panel shows the temporal sequence of events plotted by latitude (vertical axis=latitude, horizontal axis = JD). Uptick in seismicity associated with the Esmeraldas and Atacames swarms labeled. Note uptick in seismicity, both number of events and magnitudes throughout the margin during the time period of the Esmeraldas swarm, ~JD 187-195. Circles scaled and color coded by magnitude: yellow $M_w \geq 6$, orange $6 > M_l \geq 5$, brown $5 > M_l \geq 4$, red $M_l < 4$. Locations of pairs of $M \geq 6$ events (yellow circles) from the automatic catalog, $M_w$ from NEIC (2017): 4/20/16: $M_w$ 6.2 and 6.0; 4/22/16: $M_w$ 6.0 and 5.9; 5/18/16: $M_w$ 6.7 and 6.9; 7/11/16: $M_w$ 6.3 and $M_l$ 6.0, $M_w$ 5.9). See Figure 1 for topography and bathymetry scaling.

for the northern and southern clusters. We assessed how much the depth estimates vary between fixed- and free-depth solutions by comparing results from a subset of events located using near-source phases only for which we were able to obtain free-depth solutions (Figure S7). We observe relatively good agreement between the depth estimates obtained from the fixed- and free-depth solutions. The depth differences between fixed- and free-depth solutions range from ±0.03 to ±5.0 km with the majority of events having depth differences smaller than ±2 km.

## 4. Results

### 4.1. The Pedernales Sequence: Earthquake Catalog

The initial catalog using the processing sequence described in section 2.2 contained 18,809 events from 17 April 2016 (JD 2016:108) to 31 August 2017 (JD 2107:243). Manual review of events and waveforms indicates that events with eight phases are reliably earthquakes. Earthquakes were detected and located with less than eight phases, but the number of spurious signals being associated as local events is higher. For the purpose of studying the spatio-temporal evolution and characterizing the Pedernales sequence, we focus on a catalog of high-quality locations requiring a minimum of eight phases and horizontal and depth errors less than or equal to 10 km. The resulting dataset contains 9,036 events between 17 April 2016 (JD 2016:108) and 4 July 2017 (JD 2017:185), the last day that stations in the temporary network detected events (Figure 2). Magnitudes in the catalog range from Ml 0.6 to 6.4 with a magnitude completeness (Mc) of 2.3 (Figure S8). The catalog is available in QuakeML format in the supporting information.

The majority of earthquakes occur at depths shallower than 36 km (Figure S8). Airquakes (earthquakes that locate above sea level) are set to 0-km depth. Earthquakes locating deeper than 100 km are set to 100-km

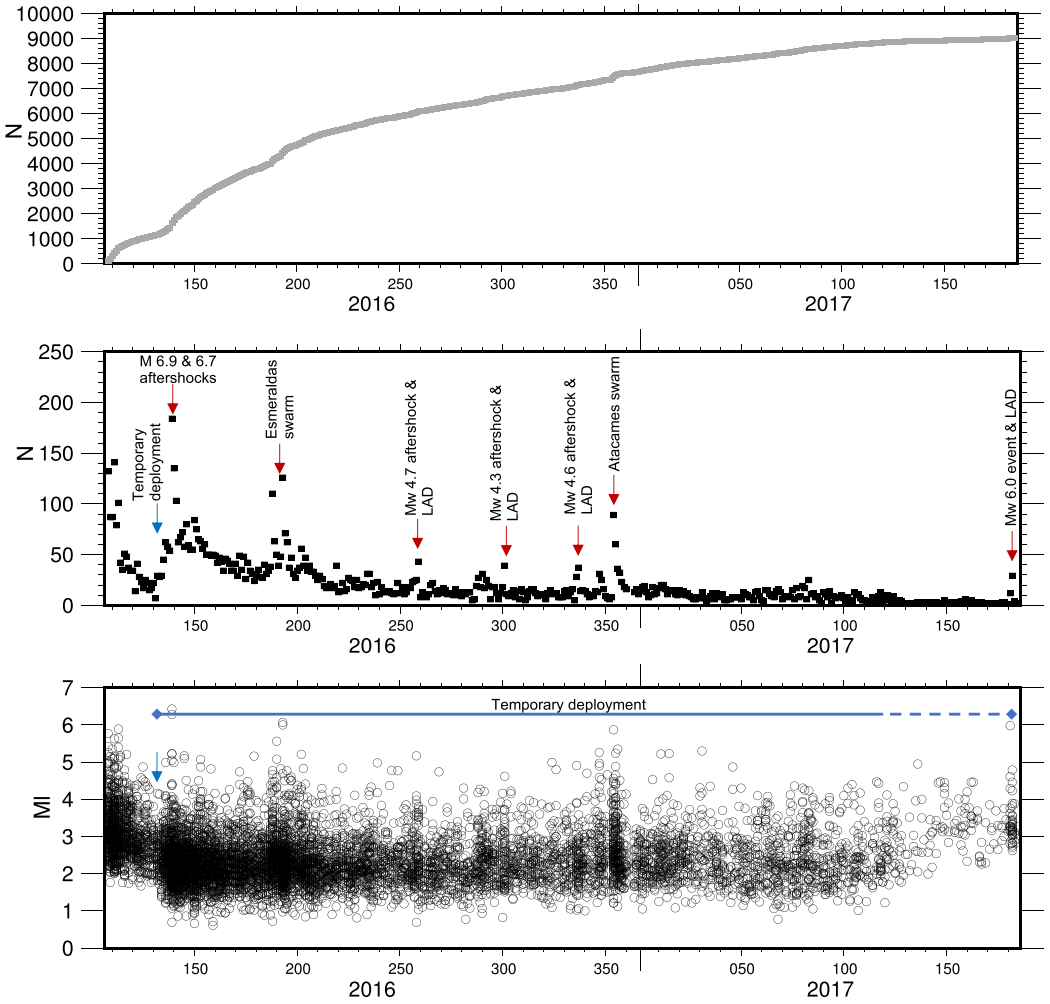


**Figure 3.** (top) Cumulative number of events, (middle) number of events per day, and (bottom) event magnitude per day from automatic catalog 17 April 2016 (Julian day [JD] 2016:108) to 4 July 2017 (JD 2017:185), minimum of eight phases and errors less than 10 km, $n$=9036 events. The horizontal axis is JD. The red arrows mark increases in seismicity associated with large magnitude aftershocks that generate their own local aftershock decay (LAD) and the Esmeraldas and Atacames swarms. The blue arrow notes beginning of temporary deployment. Note the increase in number of events detected and decrease in magnitude threshold as the number of stations increased. The blue bar and diamonds mark main time period of temporary deployment, the solid line marks the main deployment. Only a handful of temporary stations remained in the field past May 2017 (dashed line). Note the decrease of number of events detected and increase in magnitude threshold after May 2017 as number of stations decreased.

depth. Most earthquakes were located using 8 to 36 phases (Figure S8). Histograms of location errors using 68% confidence ellipses are provided in Figure S8. The average length of the semimajor axis is 1.92 km with a standard deviation of 1.3. The average length of the semiminor axis is 0.90 km with a standard deviation of 0.45. The average depth error is 0.93 km with a standard deviation of 1.17 km. These formal uncertainties do not reflect any bias introduced by using a 1-D global velocity model in a region with 3-D velocity heterogeneity.

The spatial distribution of events shows a clear pattern of clustering within, around, and to the north and south of the rupture (Figure 2). The cumulative number of events, number of events per day, and the daily distribution of earthquake magnitude indicate a high rate of seismicity that gradually decays with time (Figure 3 and animation in the supporting information). Superimposed on this gradual decay are bursts of activity, focused higher rates of seismicity, lasting from several days to up to a week, or more. The reversal in seismicity rate decay observed near JD 2016:130, and the coincident step decrease in the lower limit of

magnitudes recorded coincides with the deployment of temporary stations on land. The increase in number of events and decrease in magnitude threshold highlights the importance of dense deployments to capture aftershock sequences. Higher magnitude events ($5 \leq M \leq 7$) are interspersed throughout the postseismic sequence up to 9 months after the mainshock (Figure 3). The two largest aftershocks (Mw 6.9 and Mw 6.7; NEIC, 2016a, 2016b) occurred on JD 2016:139 and were followed by an increase in the level of seismicity (Figures 2 and 3). An increase in the seismicity rate on JD 2016:187 and JD 2016:354 corresponds to the initiation of earthquake swarms in the northern Esmeraldas and Atacames region (Figures 2 and 3). From the end of January 2017 through the end of the temporary deployment, the magnitude and frequency of events decay to background levels associated with the interseismic period.

### 4.2. The Pedernales Sequence: Calibrated Relocations

Using HDC, 72 of the 89 M>4.0 events, including the foreshock and mainshock, met the selection criteria and were relocated; 48 events were relocated in the northern cluster and 24 events in the southern cluster (Figure 4 and Table S1 supporting information). Inversions using the remaining 17 of the 89 events were unstable so these events were excluded from the inversion. A total of 16,843 phases were used to calculate the cluster vector locations for the northern cluster, while 4,140 phases were used for the southern cluster. The majority of large aftershocks ($M > 6.0$) locate in the northern cluster resulting in the large difference in the number of phases between the northern and southern clusters. Calibrated locations systematically shift west (Figure 4) with respect to initial locations. The change in location ranges from 1 to 38 km. Travel time residuals for near-source phases average 0.1 s for Pg and -0.2 s for Sg for the northern cluster and −0.2 (Pg) and −0.1 (Sg) for the southern cluster (Figure S9). The mean length of the cluster vector error ellipse semi-major axis is 1.57 km for the northern cluster and 1.97 km for the southern cluster (Figure S10). The change in location of the calibrated relocations is much larger than these uncertainties.

## 5. Discussion

### 5.1. The Pedernales Earthquake: Foreshock and Mainshock

The determination of accurate, absolute locations of large subduction earthquakes is essential to model the initiation and evolution of coseismic slip, to characterize postseismic activity, and to assess seismic hazard. Hypocenter locations for the foreshock and mainshock from the USGS-NEIC (2016c), Nocquet et al. (2017), Ye et al. (2016), and our calibrated locations using the HDC method are compared in Figure 5. Epicentral locations are separated by 20 to 40 km. Locations relying primarily on teleseismic data (NEIC, 2016; Ye et al., 2016) locate east beneath the coast while those using local phases (Nocquet et al., 2017; this study) locate west offshore. The calibrated location obtained in this study lies closer to those of Nocquet et al. (2017), reflecting the incorporation of local phases into the location.

The position of the top of the slab from two models, Slab2 (Hayes et al., 2018) and 3DVM (Font et al., 2013), is plotted for reference (Figure 5). In Ecuador, Slab2 makes use of earthquake hypocenters and an average plate interface depth from active source data (Hayes et al., 2018). The slab position in 3DVM is derived from an a priori 3-D *P*-wave velocity model constructed from geophysical data (active source, earthquake hypocenters, and gravity) and geologic studies along the Ecuadorian margin (Font et al., 2013). The top of the slab in the two models diverges with distance from the trench. In Slab2, a steeper dip to the subducting slab results in the top of the plate interface being up to ~15 km deeper than the top of the slab from 3DVM at the eastern termination of seismicity associated with the Pedernales sequence. The depth of the mainshock using the HDC relocation method and the NEIC location coincide with the plate interface from the 3DVM (Font et al., 2013). The depth obtained by Nocquet et al. (2017) is between the 3DVM and Slab 2.0 model.

### 5.2. The Pedernales Sequence: Spatial Distribution of Seismicity

The Pedernales seismic sequence is dominated by pronounced spatial clustering and a striking downdip limit in seismic activity. Most of the events locate outside the rupture area of the main shock (Figure 2; Meltzer et al., 2019; Agurto-Detzel et al., 2019; León-Ríos et al., 2019). Three apparent bands of seismicity run perpendicular to the strike of the trench: the Jama band updip from the southern end of the rupture, the Cojimies-Atacames Seamount band approximately coincident with the northern end of the rupture, and the Galera band approximately 20 km north of the rupture (Figure 2). Seismicity is noticeable reduced between these apparent bands. On closer inspection, and as described in section 5.3, seismicity within these

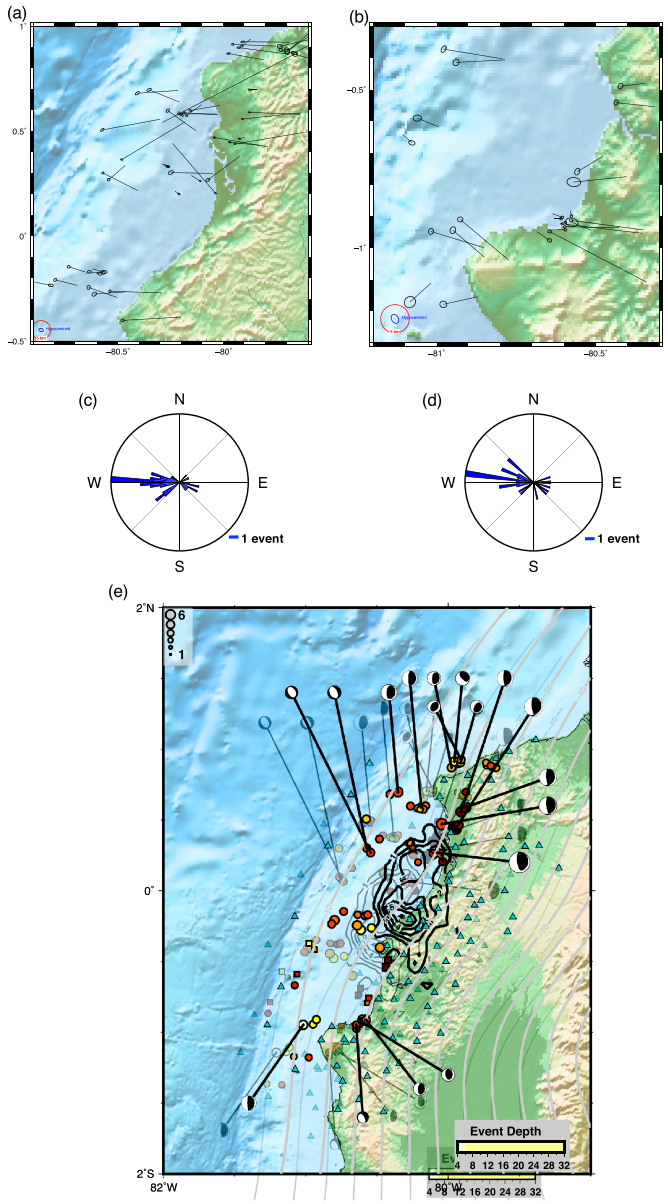


**Figure 4.** Hypocentroidal decomposition event relocation: (a) northern cluster and (b) southern cluster. The error ellipse is placed at the final location; the vector connects to the initial location. Error ellipse scale bar (5 km) lower left, (red circle). The rose diagram of relocation vectors: (c) northern cluster ad (d) southern cluster; the scale bar equal to one event is shown beneath each diagram. (e) Map of relocated events ($N$=72) color coded by event depth and scaled by magnitude. Mainshock and foreshock stars, postseismic events in the Pedernales sequence circles, pre-Pedernales events from interseismic coupling catalog squares. Slab contours every 10 km from Slab 2.0 (Hayes et al., 2018). gCMT and NEIC-RMT solutions available for 18 of the 72 relocated events are shown. Note that the majority of events are thrust mechanisms; three events show normal faulting, two where the Atacames seamounts subduct (Marcaillou et al., 2016) and one in the Manta region. Topography and bathymetry scaling and Pedernales coseismic slip contours as in Figure 1. Station distribution as in Figure 2.

bands occurs in distinct individual clusters in space and time. As such, the apparent banding observed in Figure 2 is best considered as a composite cluster composed of individual focused clusters. These patterns exist despite the limitation of locating events with a 1-D velocity model. Preliminary results from a joint inversion for earthquake location and 3-D velocity structure show that individual earthquakes within the clusters shift and focus, but the location of the composite clusters themselves does not shift (Hoskins et al., 2019).

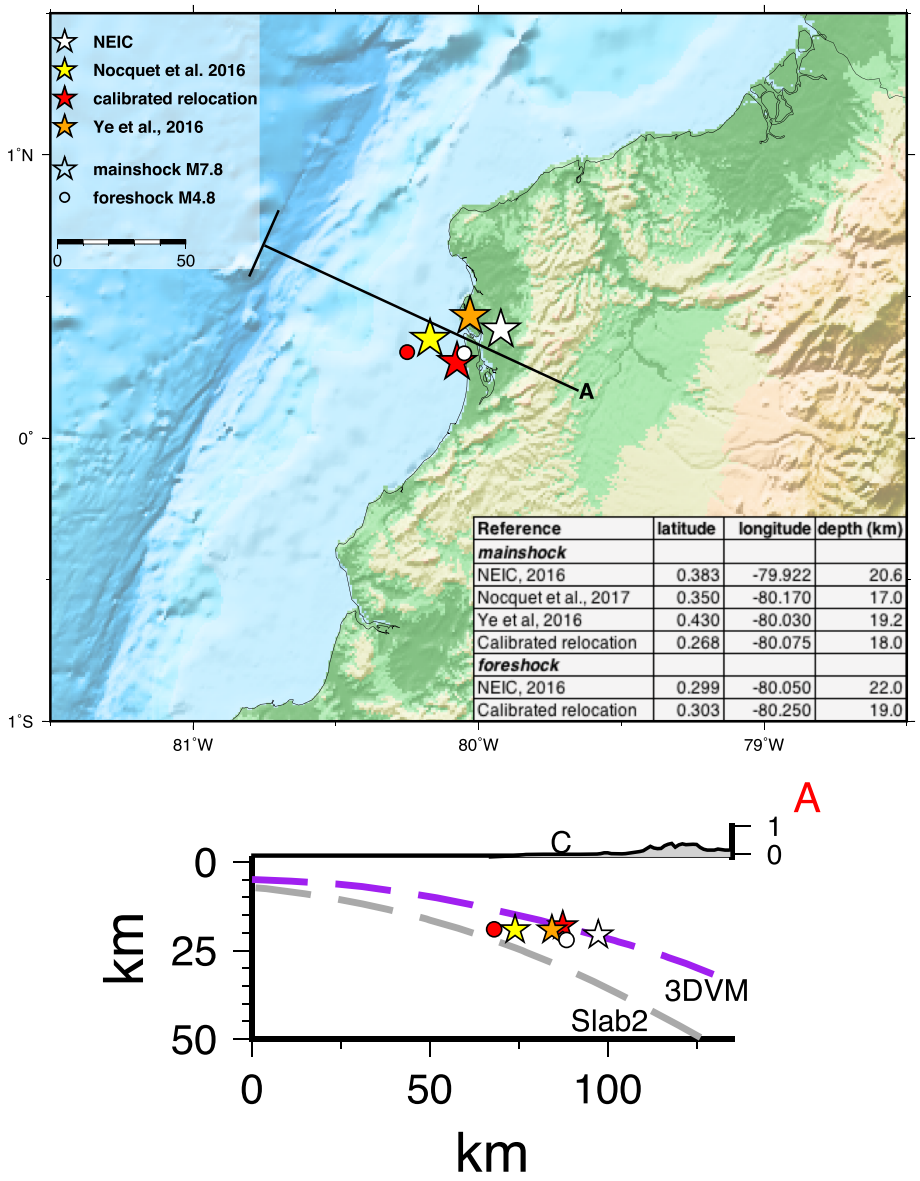


**Figure 5.** Comparison of Pedernales mainshock and foreshock locations from various studies. Top map view hypocentroidal decomposition relocation red, NEIC (2016) white, Ye et al. (2016) orange, and Nocquet et al. (2017) yellow. Distances between epicentral locations range from 20 to 40 km. Bottom, cross section. Slab models from 3DVM (Font et al., 2013) purple dashed line and Slab 2.0 (Hayes et al., 2018) gray dashed line. Topography above sea level plotted in gray above cross section; coastline marked by C. Hypocentroidal decomposition relocation of mainshock falls along the plate interface based on the 3DVM slab model.

Seismicity is observed west of the trench (western end of the Jama and Cojimies-Atacames Seamount composite clusters) where topography on the Carnegie Ridge and the Atacames Seamounts subduct beneath the trench. Aftershocks are also focused within the rupture area where a patch of low slip separates two patches of larger slip. Seismicity is spatially focused ~50 km to the south of the rupture in the Manta-Puerto Lopez composite cluster (including the individual Manta, Jipijapa, and San Lorenzo clusters). Onshore a prominent band of seismicity extends north from the northeast end of the rupture. This band, like others in the Pedernales sequence, is made up of individual clusters of seismicity near Muisne, Atacames, and farther northeast near Esmeraldas. Calibrated relocations (Figure 4) show a similar focusing of events and the sharp eastward termination of seismicity visible in the full catalog.

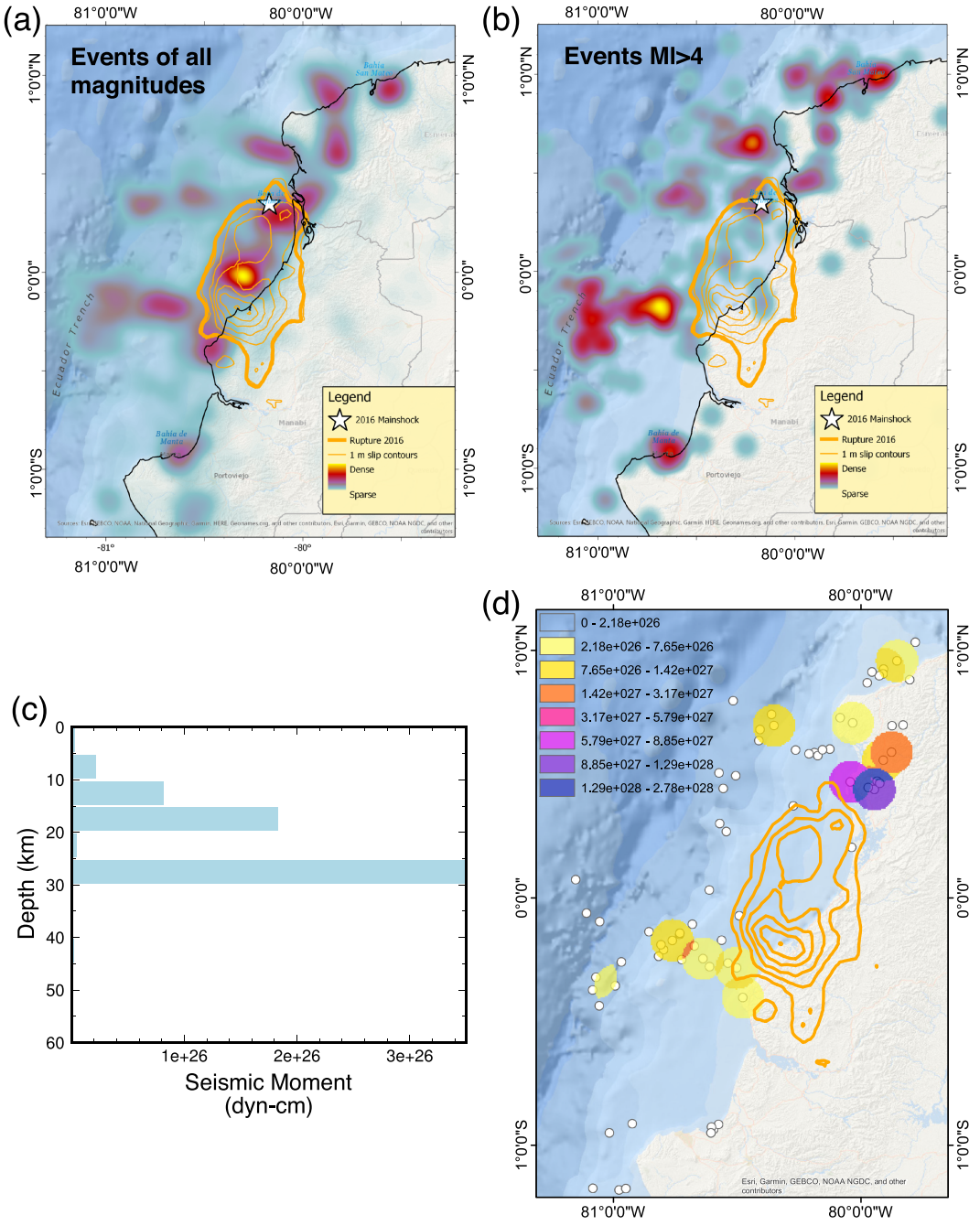


**Figure 6.** Density distribution of seismic events in the Pedernales sequence automatic catalog. (a) Events of all magnitudes (9,036 events); (b) events $M_l \geq 4$ (308 events) using the kernel density function within Esri ArcGIS Pro©. (c) Depth distribution of cumulative seismic moment (dyn-cm) for aftershocks $M_w \geq 4.56$, $M_l \geq 4.64$ (85 events). (d) Seismic moment density plot for aftershocks $M_w \geq 4.56$, $M_l \geq 4.64$ (85 events) using the point density function within Esri ArcGIS Pro©. Maximum moment release between 25 and 30 km is associated with the series of $M \geq 6.0$ events near the plate interface.

While the largest number of events occurs within the low-slip region between the two patches of maximum coseismic slip, these are small magnitude events (Ml ≤4.0; Figures 2 and 6). The larger magnitude events (Ml ≥ 4) generally occur within clusters outside of the rupture area (Figures 2, 4, and 6). An absence of moderate to large aftershocks within the mainshock high-slip zones is observed in the wake of a number of megathrust ruptures (Agurto et al., 2012; Wetzler et al., 2018). Events with Ml ≥ 5 occur exclusively outside the rupture

area (Figures 2 and 4). Ml ≥ 6 aftershocks are restricted to focused regions. These larger magnitude aftershocks occur north and northeast (downdip) of the end of the rupture in the vicinity of the eastern end of the Galera composite cluster. They also occur at the very southern end of the rupture on the eastern end of the Jama composite cluster (Figures 2 and 4). The Ml ≥ 6 events occur in pairs minutes to hours apart. Seismic moment for the 86 largest postseismic events range from 8.64E+22 to 2.81E+26 dyne-cm (Mw 4.56–6.90). Cumulative seismic moment of the aftershocks concentrates between 25- and 30-km depth (Figure 6c). Moment release associated with the aftershocks is dominated by the Mw ≥ 6.0 event pairs that occurred on 18 May 2016 and 11 July 2016 (Figure 6d). An additional concentration of moment release is associated with the Jama composite cluster, south and updip of the southern end of the rupture. North of the rupture, concentrations of moment release occur at the western end of the composite Galera cluster and in the Atacames-Esmeraldas region (Figure 6d).

Cross sections perpendicular to the trench illustrate the focused clustering of seismicity in space and time and the distribution of seismicity with depth along strike (Figure 7). Earthquakes exhibit an abrupt termination approximately 80 km east of the trench where event depths reach 30–35 km. Events locate along the plate interface, in the upper plate, and in the subducting slab. Both plate models, Slab 2.0 (Hayes et al., 2018) and 3DVM (Font et al., 2013), are shown on the cross section. In places, the distribution of seismicity is more consistent with either the 3DVM model or the Slab 2.0 model. In places, it is not consistent with either model. Despite the discrepancy in the plate interface models, clear patterns emerge in the depth distribution of seismicity along strike and dip (see Figure S11 in the supporting information for detailed descriptions of the cross sections). In almost all instances, Ml ≥ 5 earthquakes occur at depth close to the plate interface, while events Ml < 5 occur at a range of depths. There is a clear transition from seismicity focused almost exclusively in the upper plate north of the rupture to seismicity either broadly distributed or primarily bracketed by the two plate models along strike to the south. (Figure 7). The base of seismicity in both the Esmeraldas and Atacames clusters (Figure 7 cross section A and B) is consistent with the 3DVM slab model of Font et al. (2013), whereas in the Muisne cluster (Figure 7 cross section C), it is more consistent with the Slab 2.0 model. Seismicity in the three composite clusters (Figure 7, cross sections D, F, and H) is generally bracketed by the two plate interface models. Where the Atacames Seamounts and Carnegie Ridge enter the trench, there is abundant seismicity in the lower plate (Figure 7, cross sections F and H). Seismicity in the rupture zone occurs between the two patches of larger slip and is vertically distributed between 5- and 25-km depth (Figure 7, cross section G). Seismicity to the south in the Manta-Puerto Lopez composite cluster (Figure 7 cross section I) concentrates at depths of 15 to 30 km, suggesting that seismic activity occurred in the lower part of the overriding plate and the uppermost part of the downgoing plate.

### 5.3. The Pedernales Sequence: Temporal Evolution

The Pedernales sequence exhibits spatially focused higher rates of seismicity superimposed on the general decay in earthquake frequency and magnitude with time after the mainshock (Figures 3 and 8 and animation in the supporting information). These bursts in seismicity last from several days to weeks and take place intermittently over the first nine months after the mainshock. This seismicity forms the clusters observed in map view and cross section (Figures 2 and 7). The bursts in seismicity generally take two distinct forms, occurring either as earthquake swarms or as larger magnitude aftershocks followed by a local decay in event frequency and magnitude (local aftershock decay) over a period of several days. In contrast, earthquake swarms are identified by an increase in spatially and temporally clustered seismicity, with a range of earthquake magnitudes distributed throughout the cluster, and the highest magnitude events occurring within the time period of the swarm rather than at the beginning (Holtkamp & Brudzinski, 2011). The evolution of the Pedernales Sequence is described below and shown in the animation in the supporting information. Additional details of the temporal evolution are included in Text S1 in the supporting information.

#### 5.3.1. 17 April to 8 May 2016 (JD 2016:108–129), Days 1–22 After the Mainshock

For the first 3 weeks after the mainshock, postseismic activity was only recorded by the permanent stations of the national seismic network. This time period coincides with the initiation and growth of the two patches of afterslip updip north and south of the rupture (Figure 9; Rolandone et al., 2018). Mw ≥ 5aftershocks within this time period occur within the first 10 days after the mainshock. These events primarily locate

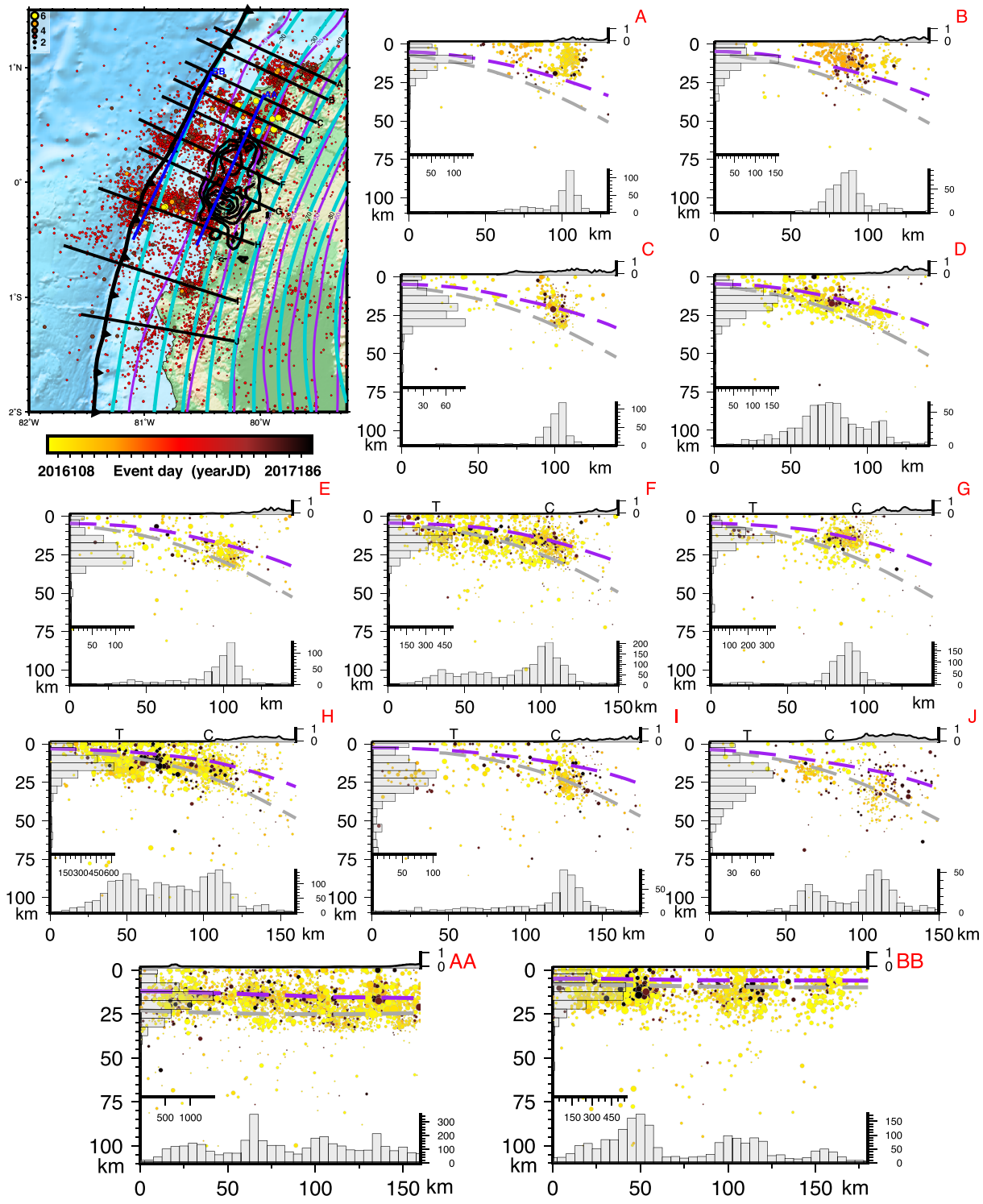


**Figure 7.** Depth distribution of seismic events contained in the Pedernales sequence automatic catalog. (a) Cross sections locations. Black lines, sections A–J perpendicular to trench axis across main composite clusters. Hypocenters from 10 km on either side of the transect projected onto line of section A through E and G; hypocenters from 20 km on either side of the transects F, I, and J projected onto line of section; hypocenters from 30 km on either side of the transect H projected onto line of section. White lines, sections AA and BB approximately parallel the trench, subducting slab, and coast; hypocenters from 30 km on either side of the transect projected onto line of section. Gray contours every 10 km plate interface Slab 2.0 (Hayes et al., 2018), purple contours every 10-km plate interface 3DVM (Font et al., 2013). Left panel: Cross sections with events scaled and color coded by magnitude: yellow $M_w \geq 6$, orange $6 > M_l \geq 5$, brown $5 > M_l \geq 4$, red $M_l < 4$. Right panel: Cross sections color-coded by time. Histograms show the distribution of events by depth (vertical axis) and by distance (horizontal axis. Topography shown above sea level. T marks location of trench, C marks the coastline. Dashed line plate interface, gray Slab 2.0 (Hayes et al., 2018), purple 3DVM (Font et al., 2013).

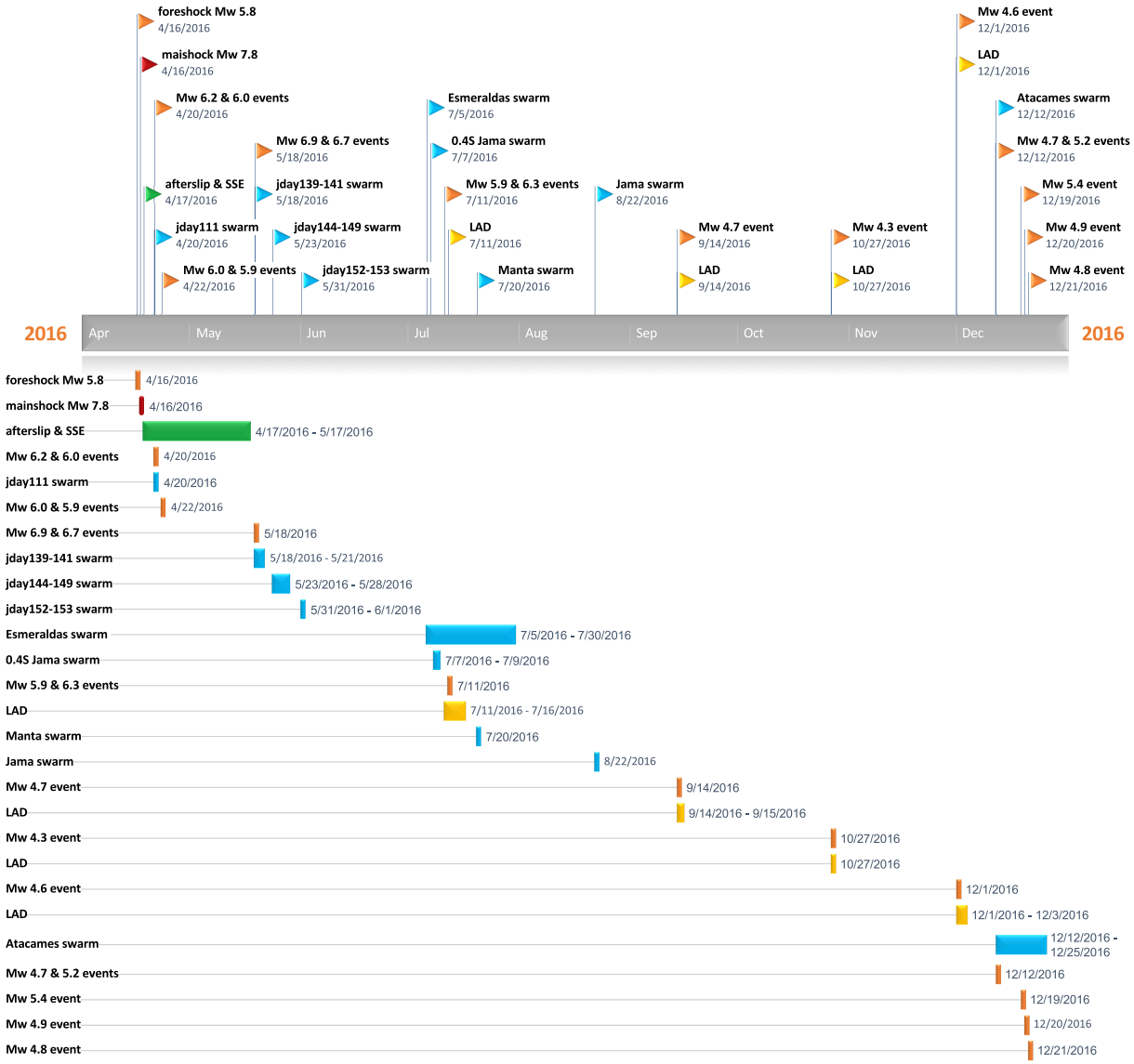


**Figure 8.** Timeline of Pedernales sequence 16 April 2016 through 31 December 2016. The top bar denotes initiation of event(s), foreshock (orange), mainshock (red), aseismic afterslip, and slow slip event (green), larger magnitude aftershocks (orange), which initiate their own local aftershock sequence (LAD; yellow), and earthquake swarms (blue). Moment magnitudes from the NEIC (2017).

along the plate interface. This 10-day period coincides approximately with the rapid accumulation of afterslip (Rolandone et al., 2018). Mw $\geq$ 5 events are almost exclusively restricted to the Jama and Galera composite clusters. During this 10-day interval, these larger events occur in either the Jama or Galera composite cluster over 1- or 2-day periods; they do not occur concurrently in both composite clusters. The largest magnitude aftershocks (Mw 5.9–6.2) occur as pairs of events 2 days apart, one pair each in the Galera and Jama composite clusters.

Events in the composite clusters focus spatially and migrate in time along the fringes of the afterslip patches. Afterslip and seismicity updip adjacent to the rupture are noticeably lacking. The initial spatial extent of afterslip in the southern patch is small, whereas seismicity is widely distributed in an east-west band north of the afterslip that forms the Jama composite cluster (Figure 9a). As the southern patch of afterslip grows, seismicity is more focused toward the west and at the trench (Figure 9b). Larger magnitude events in the Jama composite cluster occur initially when the spatial extent of afterslip in the southern patch is quite small and occur again as the southern patch continues to expand and accumulate slip. Six days after the

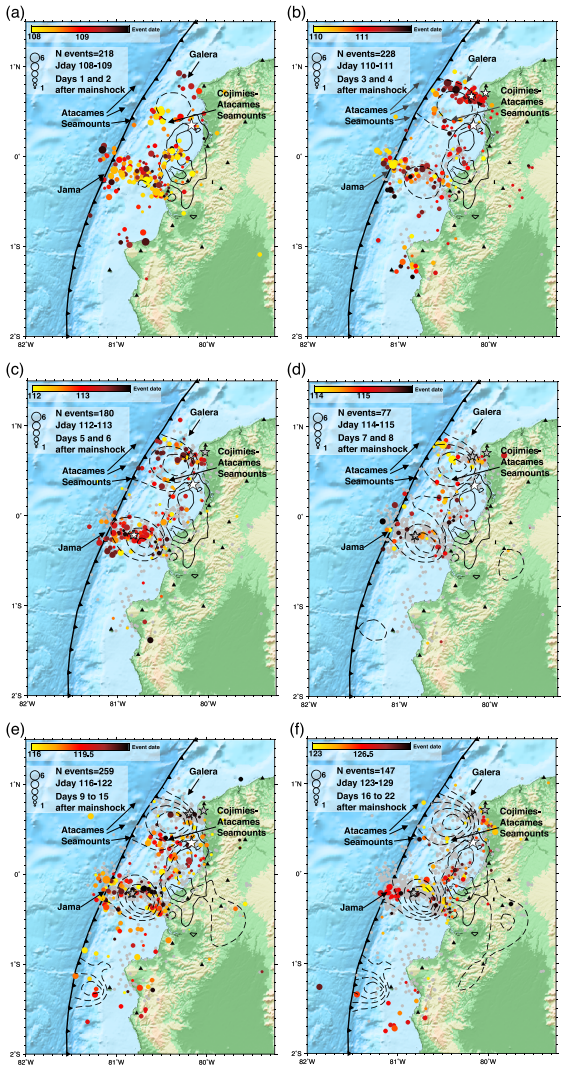


**Figure 9.** The Pedernales sequence 17 April to 8 May 2016, days 1–22 after the mainshock (JD 2016:108–129). Events scaled by magnitude and color-coded by time within each panel, (a–d) 2 days and (e–f) 7 days. Julian day (JD) range and total number of events included in each panel. The dashed contours indicate the cumulative aseismic slip (afterslip and SSEs), 10-cm contour interval (Rolandone et al., 2018). The large white star indicates the mainshock epicenter; continuous contours coseismic slip 1-, 3-, and 5- m contours (Nocquet et al., 2017). The black triangles indicate the IGEPN coastal stations from permanent network recording during this time interval. Atacames seamounts labeled with black arrows. Composite clusters labeled with black arrows. (a) JD 2016:108–109, days 1 and 2 after the mainshock. (b) JD 2016:110–111, days 3 and 4 after the mainshock, white stars $M_w \geq 6$ aftershocks in the Galera composite cluster. (c) JD 2016:112–113, days 5 and 6 after the mainshock, white stars $M_w \geq 6$ aftershocks in the Jama composite cluster, previous $M_w \geq 6$ aftershocks in Galera composite cluster gray stars. (d) JD 2016:114–115, days 7 and 8 after the mainshock, gray stars previous $M_w \geq 6$ aftershocks for reference. (e) JD 2016:116–122, days 9–15 after the mainshock, gray stars previous $M_w \geq 6$ aftershocks for reference. (f) JD 2016:123–129, days 16–22 after the mainshock, gray stars previous $M_w \geq 6$ aftershocks for reference.

mainshock, the paired large aftershocks (Mw 6.1 and Mw 5.8) occur 17 min apart in the Jama cluster close to the area of maximum accummlated afterslip (Figures 2, 8, and 9c). In contrast the initial spatial extent of the northern patch of afterslip is larger, and seismicity is focused along the southwest edge of afterslip forming the Cojimies-Atacames Seamount composite cluster (Figure 9a). The spatial extent of the northern patch of afterslip grows rapidly and seismicity shifts and is focused along an east-west band along northern edge of the afterslip patch forming the Galera Composite cluster (Figure 9b). Larger magnitude aftershocks in the Galera composite cluster are coincident with the expansion and accumulation of afterslip. Four days after

**Table 1**
*Earthquake Swarms in the Pedernales Sequence*

| Location | Start date | Duration in days | No. of events | Magnitude range | Comments |
|---|---|---|---|---|---|
| Galera (jday 111) | 20 April 2016 | 1 | 66 | Ml 2.0 to Mw 6.2 | 15 events Ml ≥ 4.2 |
| Galera (jday 139-141) | 18 May 2016 | 3 | 36 | $M_l$ 2.0 to $M_l$ 5.0 | |
| Atacames Seamounts (jday 144-149) | 23 May 2016 | 5 | 67 | $M_l$ 2.0 to $M_l$ 4.26 | |
| Atacames Seamounts (jday 152-153) | 31 May 2016 | 2 | 57 | $M_l$ 1.6 to $M_l$ 5.07 | |
| Esmeraldas | 5 July 2016 | 25 | 210 | $M_l$ 1.6 to $M_l$ 4.5 | 12 events Ml ≥ 4.0 |
| Jama (0.4S) | 7 July 2016 | 2 | 26 | $M_l$ 1.88 to $M_l$ 5.56 | 6 events Ml ≥ 4.25 |
| Manta | 20 July 2016 | 1 | 24 | $M_l$ 1.8 to $M_l$ 5.2 | |
| Jama | 22 August 2016 | 1 | 9 | $M_l$ 1.9 to $M_l$ 4.2 | |
| Atacames (town) | 12 December 2016 | 14 | 253 | $M_l$ 1.53 to $M_l$ 5.87 | 21 events $M_l$ ≥ 4 |

the mainshock, an earthquake swarm occurs in the Galara cluster (Figure 9b and Table 1). The two largest events in the swarm, Mw 6.2 and Mw 6.0 (NEIC, 2017), occur 2 min apart (Figures 2, 8, and 9b). The rate of seismicity in the composite clusters decays after the first week even as cumulative afterslip continues to increase (Figures 9e and 9f).

#### 5.3.2. 9 May to 4 July 2016 (JD 2016:130–186), Days 23–79 After the Mainshock

Between 9 May 2016 (day 23 after the mainshock) and 22 May, the temporary stations from the coordinated international rapid response effort were installed. By 31 May, the OBS stations were in place and recording data. The increase in seismicity observed during this time period is in part due to improved detection capability provided by the dense network of stations (Figure 3). The distribution of seismicity for this time period follows the same general pattern established within the first 3 weeks. Events continue to occur in the Galera and Jama composite clusters, near the trench adjacent to the Atacames Seamounts, and in the patch of low slip within the rupture (Figure 10 and animation in the supporting information). On 18 May 2016 (JD 2016:139), 32 days after the mainshock, the two largest aftershocks of the Pedernales sequence, Mw 6.7 and Mw 6.9 (NEICa and b), occurred ~8 hr apart. The larger magnitude event occurs second. The events locate on the plate interface, northeast and downdip of the mainshock, and the northern patch of aseismic slip (Figure 10b and animation in the supporting information). These large aftershocks initiate their own cascade of events in the vicinity of their hypocenters and triggered an earthquake swarm offshore in the Galera cluster (Figure 10b). Within the next 2 weeks, two earthquake swarms occurred where the Atacames Seamounts intersect the trench (Figure 10c and Table 1). This area correlates spatially with the southern edge of the northern patch of aseismic slip. Two of the largest earthquakes in the second swarm have normal focal mechanisms. This is in contrast to the majority of focal mechanisms in the Pedernales sequence, which are thrust (Figure 4; see section 5.4.1 for discussion of focal mechanisms). For both these swarms, events occur primarily in the lower plate or near the plate interface (Figure 7, cross section F).

#### 5.3.3. 5 July to 25 December 2016 (JD 2016:187–360), Days 80–253 After the Mainshock

During this time period, seismicity is broadly distributed following the same patterns that characterize the earlier postseismic sequence (Figures 11–13 and Text S1, and animation in the supporting information). The number of events per day continues to decrease except for bursts of focused seismicity associated with earthquake swarms and larger magnitude aftershocks (Table 1). On 5 July 2016 (JD 2016:187) 11 weeks after the mainshock, an earthquake swarm initiated in the Esmeraldas region, ~90 km to the northeast of the mainshock rupture (Figures 8 and 11a and Table 1; Hoskins et al., 2018). Esmeraldas is in an adjacent segment of the subduction zone and close to the epicenter of the 1958 Mw 7.7 earthquake. The Esmeraldas swarm lasted several weeks, and earthquakes locate within the upper plate (Figures 11 and 7 cross section A; Hoskins et al., 2018). Coincident with the time period of the Esmeraldas swarm, an increase in seismicity is observed throughout the margin (Figures 2 and 11); an earthquake swarm occurs on the west end of the Jama composite cluster close to the trench, and two large aftershocks, Mw 5.9 and Mw 6.3 (NEIC, 2017) occur 10 min apart on 11 July (Figure 11b). The larger magnitude aftershock occurs second. These large aftershocks occurred ~16 km north of the two large 18 May aftershocks, at depths coinciding with the plate interface. In December 2016 (10–25 December, JD 2016:354–360), 8 months after the mainshock, a significant increase in seismicity is observed ~70 km north of the mainshock near the town of Atacames (Figures 8 and 13 and Table 1, and animation in the supporting information). Atacames is in an adjacent

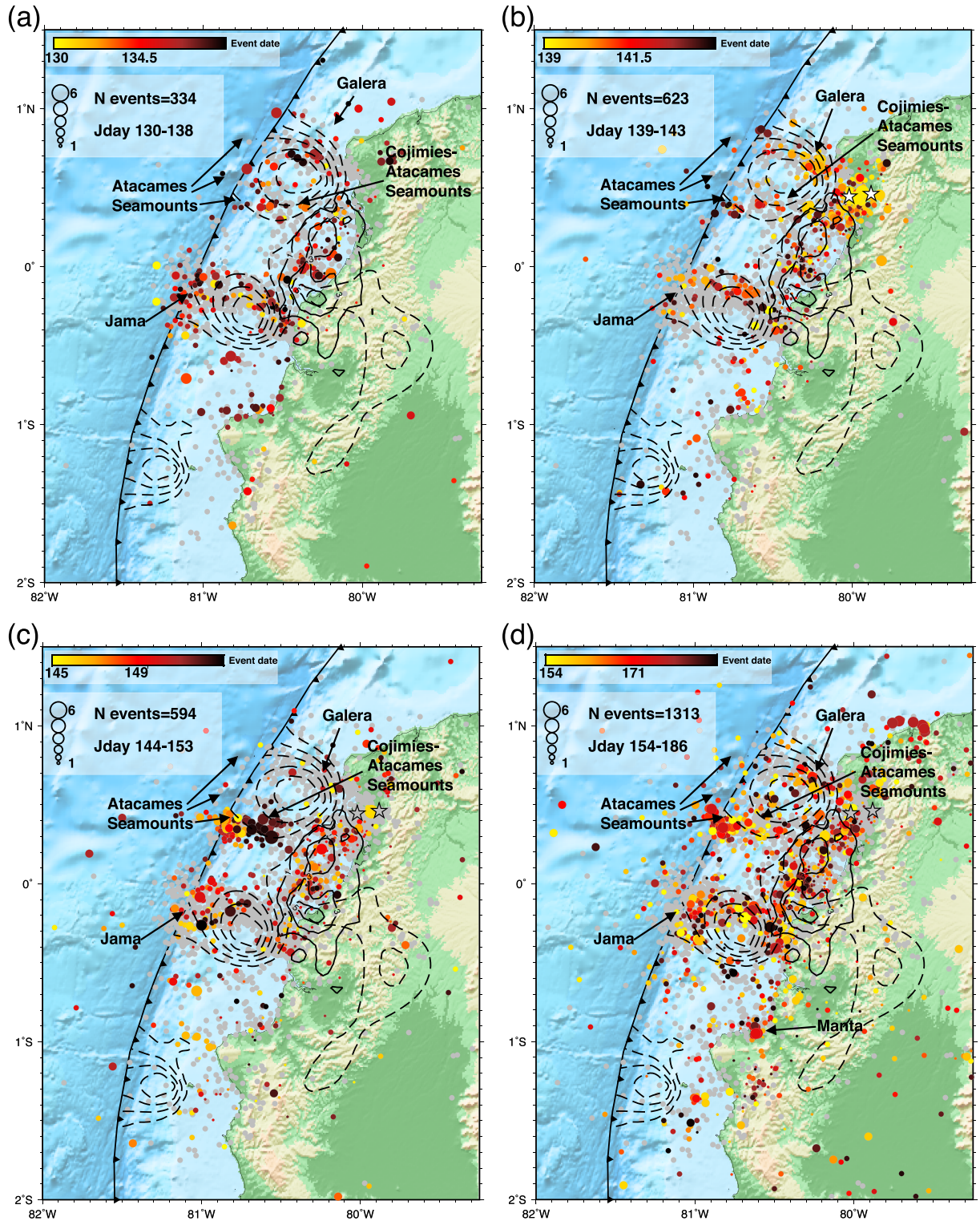


**Figure 10.** The Pedernales sequence 9 May to 4 July 2016, days 23–79 after the mainshock (Julian day [JD] 2016:130–186). Events scaled by magnitude and color-coded by time within each panel. JD range and total number of events included in each panel. Atacames seamounts labeled with black arrows. Composite clusters labeled with black arrows. (a) 9 days JD 2016:130–138, gray stars previous $M_w \geq 6$ events. (b) 5 days JD 2016:139–143, white stars $M_w$ 6.9 and 6.7 events. (c) 10 days JD 2016: 144–153, gray stars previous $M_w \geq 6$ events. (d) 33 days JD 2016:154–186, gray stars previous $M_w \geq 6$ events. The dashed contours indicate the cumulative aseismic slip (afterslip and SSEs) over the first 30 days shown for reference; 10-cm contour interval (Rolandone et al., 2018). Continuous contours coseismic slip 1-, 3-, and 5-m contours (Nocquet et al., 2017).

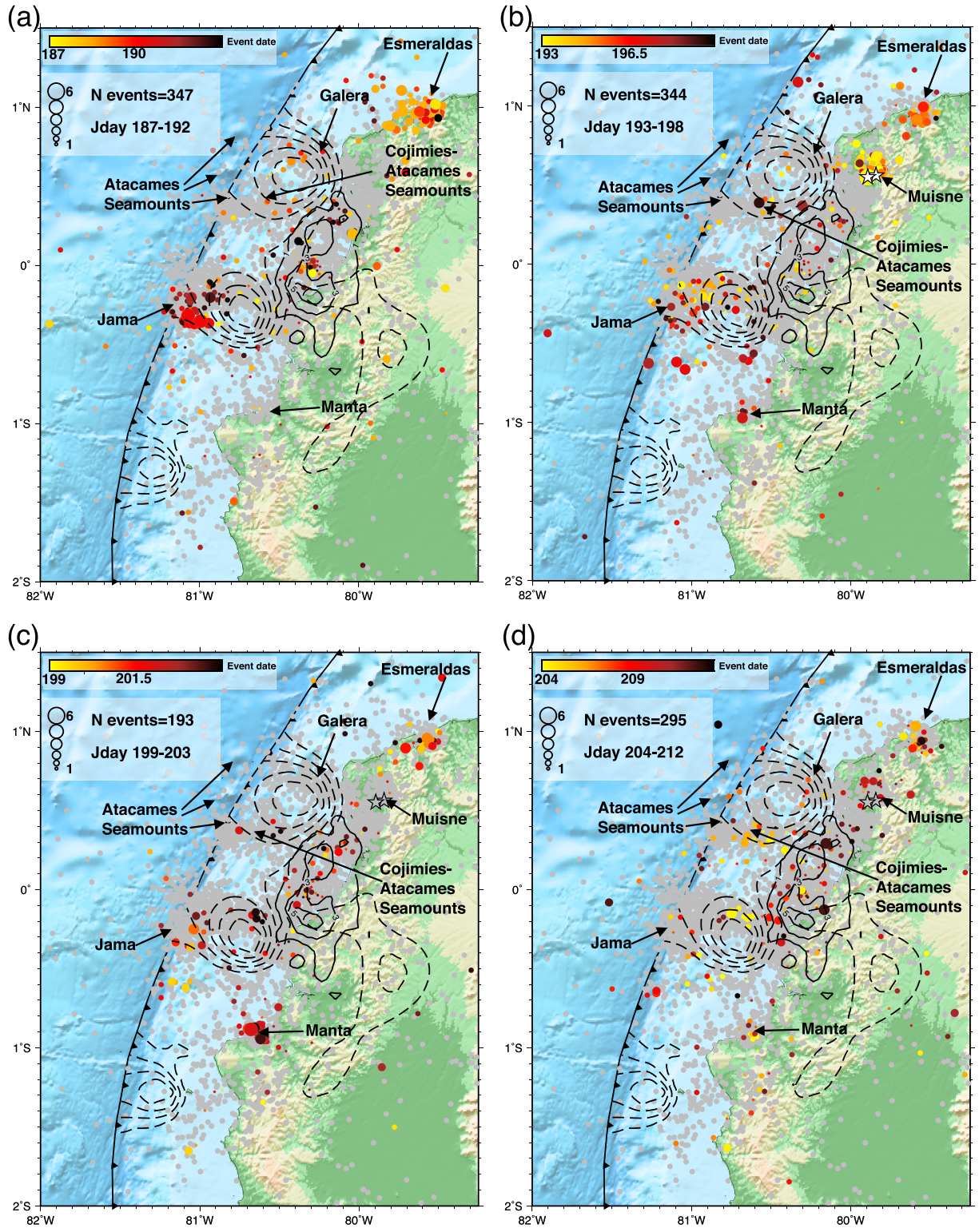


**Figure 11.** The Pedernales sequence 5 July to 30 July 2016, days 80–105 after the mainshock (Julian day [JD] 2016:187–212) including the Esmeraldas swarm. Events scaled by magnitude and color-coded by time within each panel. JD range and total number of events included in each panel. Atacames seamounts labeled with black arrows. Composite clusters labeled with black arrows. (a) 6 days JD 2016:187–192. (b) 6 days JD 2016:193–198, white stars $M_w \geq 6$ events (c) 5 days JD 2016:199–203, gray stars previous $M_w \geq 6$ events. (d) 9 days JD 2016:204–212, gray stars previous $M_w \geq 6$ events. The dashed contours indicate the cumulative aseismic slip (afterslip and SSEs) over the first 30 days shown for reference, 10-cm contour interval (Rolandone et al., 2018). Continuous contours coseismic slip 1-, 3-, and 5-m contours (Nocquet et al., 2017).

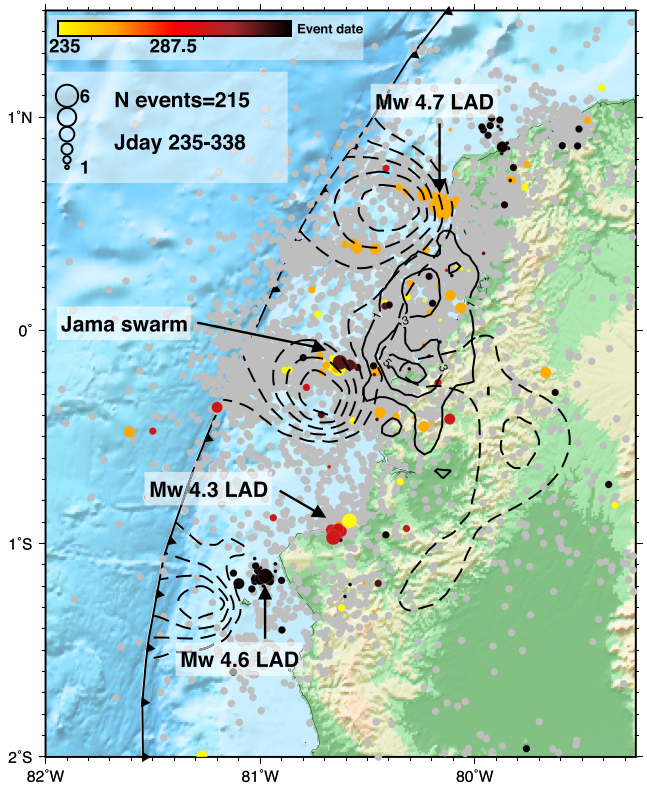


**Figure 12.** The Pedernales sequence 22 August to 3 December 2016, days 128–231 after the mainshock (JD 2016:235–338). Events scaled by magnitude and color-coded by time. Local earthquake swarm and moderate earthquakes and their local aftershock decay (LAD) labeled. The dashed contours indicate the cumulative aseismic slip (afterslip and SSEs) over the first 30 days shown for reference, 10-cm contour interval (Rolandone et al., 2018). Continuous contours coseismic slip 1-, 3-, and 5-m contours (Nocquet et al., 2017).

segment of the subduction zone and close to the epicenter of the 1906 Mw 8.8 earthquake. Over 250 events occur within the Atacames cluster in 16 days. The majority of events occur in the upper crust (Figure 7 cross section B). The Atacames sequence is best characterized as a swarm (Hoskins et al., 2018). Magnitudes range from Ml 1.53 to Ml 5.87 (Mw 5.4; NEIC, 2017), and the largest magnitude events occur within the sequence.

#### 5.3.4. 1 January 1 to 4 July 2017

During the first 6 months of 2017, seismic activity gradually decreased to background levels (Figure 3). A 2-day (30 June to 1 July 2017) increase in seismic activity (39 events) was observed 14 months after the mainshock in the Jama composite cluster following a Mw 6.0 event.

### 5.4. The Pedernales Sequence: Relationship to Interseismic Seismicity and Historical Earthquakes, Aseismic Slip, and Structure

#### 5.4.1. Relationship to Interseismic Seismicity and Historical Earthquakes

Seismicity in the Pedernales sequence matches patterns observed during the interseismic phase of the earthquake cycle, as well as maximum moment release and aftershock patterns of historic earthquakes (Figure 14; Rolandone et al., 2018, Meltzer et al., 2019; Agurto-Detzel et al., 2019; León-Ríos et al., 2019). A uniform earthquake catalog produced for seismic hazard assessment in Ecuador provides a basis for placing the Pedernales seismic sequence in the context of instrumental and historic seismicity from 1587 to 2009 (Beauval et al., 2013; Yepes et al., 2016). Similar patterns of focused clusters of seismicity are observed in both the background (interseismic) seismicity and postseismic Pedernales sequence (Figures 14a and 14b; Meltzer et al., 2019, Agurto-Detzel et al., 2019). The extent to which seismicity is more focused or diffuse is in part related to station density recording the postseismic sequence and in part due to the presence or absence of earthquake swarms during the period of observation (Figure 15). Events in the Jama composite cluster during the Pedernales sequence are more pronounced than in the interseismic period and extend from the coast to west of the trench (Figure 14b). In contrast, seismicity in the Manta-Puerto Lopez region is

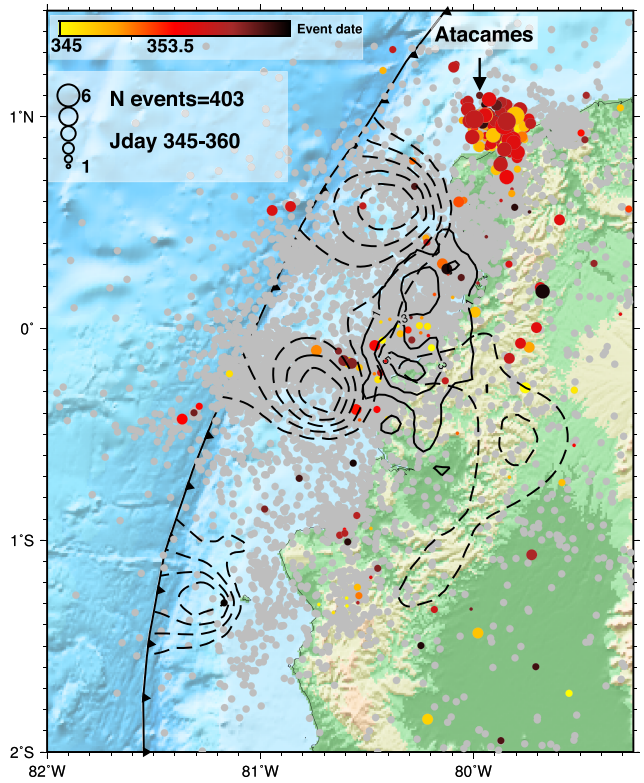


**Figure 13.** The Pedernales sequence 10–25 December 2016, days 238–253 after the mainshock (JD 2016:345–360) including the Atacames swarm. Events scaled by magnitude and color-coded by time. The dashed contours indicate the cumulative aseismic slip (afterslip and slow slip events) over the first 30 days shown for reference, 10-cm contour interval (Rolandone et al., 2018). Continuous contours coseismic slip 1-, 3-, and 5-m contours (Nocquet et al., 2017).

less pronounced in the Pedernales sequence than in background seismicity. The clusters of seismicity observed in the Pedernales sequence where the Atacames Seamounts intersect the trench are not observed in prior seismicity catalogs (Figures 14a and 14b). A prominent cluster of seismicity in the long-term catalog, west of the trench and east of a local bathymetric high on the Carnegie Ridge, is associated with an earthquake swarm in 2015 (Figures 14a and 15). Seismicity on the northeast end of the rupture is prominent in both the background seismicity and in the Pedernales sequence (Figures 14a and 14b). Seismicity extending north to Atacames and Esmeraldas is diffuse in the background seismicity catalog, but quite focused in the Pedernales sequence Figures 14a and 14b).

While the 1906 Mw 8.8 ruptured the length of the north Ecuador subduction zone, the ruptures of the Mw 7.7–7.8 and Mw 7.1 events fall within the boundaries of the composite clusters (Figure 14d). Moderate size earthquakes ($5 \leq Mw < 7$) fall almost exclusively within the composite clusters in both the interseismic period and the Pedernales sequence. This includes a series of moderate magnitude events in the Atacames and Esmeraldas area (1976 Mw 6.6, 1981 Mw 5.9, and 1989 Mw 6.3; Figure 14e).

Earthquakes preceding the 2016 Pedernales event and in the Pedernales sequence show predominantly reverse motion along north-south striking nodal planes (Figures 14b and 14e). Events in the Atacames-Esmeraldas region strike NE-SW. In the Pedernales sequence, four normal fault mechanisms are observed (Figure 14b): two where the Atacames Seamounts enter the trench, another in the Atacames-Esmeraldas region, and the forth near Manta (Jipijapa). Normal fault mechanisms are also observed in the Esmeraldas region and Manta (Jipijapa) region in the pre-Pedernales moment tensors (Figure 14e).

The relationship between interseismic coupling and seismicity varies along strike (Figure 14c; Chlieh et al., 2014; Nocquet et al., 2017; Rolandone et al., 2018; Agurto-Detzel et al., 2019). The Pedernales earthquake ruptured a moderately to highly coupled portion of the subduction zone. The highest slip patch during the mainshock rupture correlates with a highly coupled patch where seismicity is less prominent. In contrast, two highly to moderately coupled patches, immediately updip to the southwest of the rupture and downdip to the northeast, did not slip during the mainshock. These patches are seismically active during the interseismic period and are the sites of the larger magnitude aftershocks ($Ml \geq 4.0$) and higher moment release in the postseismic Pedernales sequence (Figures 6 and 14). The highly coupled patch southwest of the rupture correlates with the southern patch of afterslip. The moderately coupled patch to the northeast of the rupture is adjacent to the downdip end of the northern patch of afterslip. The seismic clusters observed where the Atacames Seamounts enter the trench correlate with a region of low coupling. The Galera and Manta Puerto-Lopez composite clusters, and seismicity north of the rupture toward Atacames and Esmeraldas, all occur at the edges of moderately to highly coupled portions of the subduction zone.

#### 5.4.2. Relationship to Aseismic Slip

There is a clear relationship between seismic and aseismic slip behaviors. Dense clusters of seismicity are associated with or border patches of the subduction zone where SSEs have been observed (Figure 14; Rolandone et al., 2018; Meltzer et al., 2019; Agurto-Detzel et al., 2019). These focused clusters of seismicity exhibit frequent earthquake swarms and repeating earthquakes (Figure 14d; Holtkamp et al., 2011; Font et al., 2013; Vallée et al., 2013; Mothes et al., 2013; Vaca et al., 2018, Segovia et al., 2018; Rolandone et al., 2018; Meltzer et al., 2019; Agurto-Detzel et al., 2019; Hoskins et al., 2018). They are also the sites of larger magnitude aftershocks. In the region from Puerto Lopez to Manta, earthquake swarms have been observed over the last several decades approximately every 3 to 5 years. SSEs were observed in 2010, 2013, and 2018 and triggered earthquake swarms along the plate interface, on secondary faults in

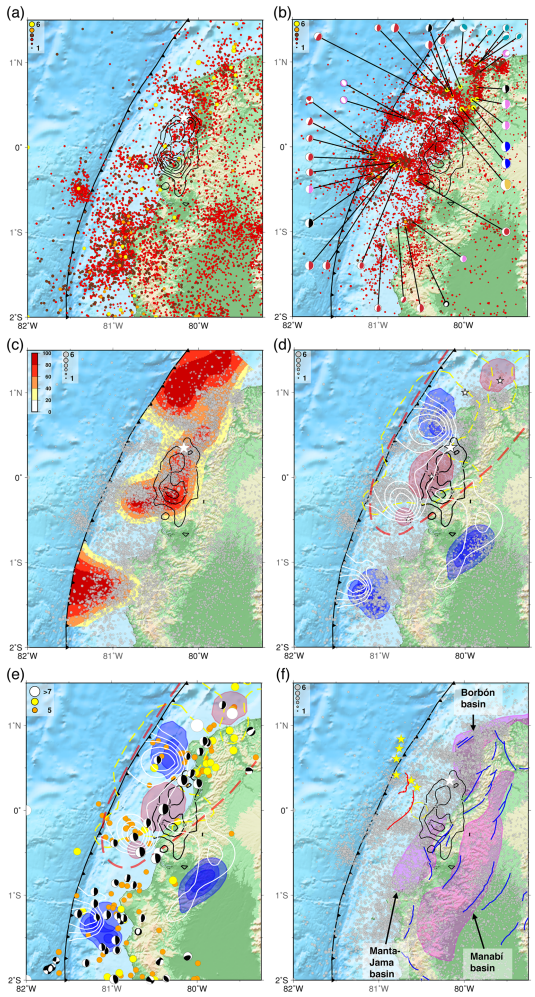


**Figure 14.** Relationship between the Pedernales sequence, interseismic seismicity, plate coupling, previous megathrust events, aseismic slip, and structure. (a) Background (interseismic) seismicity 1896 through 2009 from Beauval et al. (2013), 2011 through 16 April 2016 from IGEPN catalog. No data available for 2010. Events scaled and color coded by magnitude: yellow $M_W \geq 6$, orange 6> $M_l \geq 5$, brown 5> $M_l \geq 4$, and red $M_l$ <4. (b) Pedernales sequence, mainshock, and coseismic rupture (same as Figure 2) with moment tensor solutions from gCMT and RMT (NEIC). Moment tensors scaled by magnitude and color coded by time: 2016:4:16 (mainshock) orange, 2016:4:17 to 2016:4:26 red; 2016:5:18 (two largest aftershocks $M_W$ 6.7 and $M_W$ 6.9) blue, 2016:6:1 to 2016:8:26 violet; 2016:12:12 to 2016:12:21 cyan (Atacames); 2017 black. (c) Interseismic seismicity and Pedernales sequence, Pedernales mainshock, and coseismic rupture (from Nocquet et al., 2017), with respect to interseismic coupling (ISC) from Nocquet et al., 2014 and Collot et al., 2017. Seismicity scaled by magnitude. (d) Interseismic seismicity, Pedernales mainshock and coseismic rupture (from Nocquet et al., 2017), and Pedernales sequence with respect to previous megathrust earthquakes and aseismic slip. Epicenters white stars, areas of major moment release red shading (Beck & Ruff, 1984; Kanamori & McNally, 1982; Swenson & Beck, 1996), aftershock areas dashed yellow contours (Mendoza & Dewey, 1984). The red dashed line indicates the 1906 partial rupture area (from Collot et al., 2004). Pre Pedernales slow slip events (blue shading) and Pedernales sequence aseismic slip (afterslip and slow slip events; white contours; Vallée et al., 2013; Rolandone et al., 2018; Vaca et al., 2018). (e) Events $M \geq 5.0$ from 1896 to 4 July 2017 and gCMT and RMT (NEIC) solutions for events pre Pedernales sequence. (f) Interseismic seismicity and Pedernales sequence, Pedernales mainshock and coseismic rupture (from Nocquet et al., 2017), with respect to structure. The stars and yellow circle are locations of Atacames seamounts; the red lines are seafloor scarps, from bathymetry and seismic reflection profiles (from Marcaillou et al., 2016). Outlines of sedimentary basins purple shading (from Reyes & Michaud, 2012). Quaternary faults shown in blue (Eguez et al., 2003).

the subducting plate, and in the upper plate (Segovia et al., 2018; Vallée et al., 2013). The area where SSEs and earthquake swarms are observed is associated with topography on the subducting Carnegie Ridge. In the region associated with the Galera composite cluster, earthquake swarms and repeating earthquakes have been observed over the last several decades approximately every 1 to 4 years (Vaca et al., 2018). SSEs accompanied by earthquake swarms and repeating earthquakes were observed in 2007–2008 and 2013–2014. Earthquake swarms were observed at Galera coincident with afterslip (Figure 9) and along with repeating earthquakes continued to be observed throughout the Pedernales sequence (Figures 10–13 and Hoskins et al., 2018). Earthquakes within the swarms are observed along the plate interface and

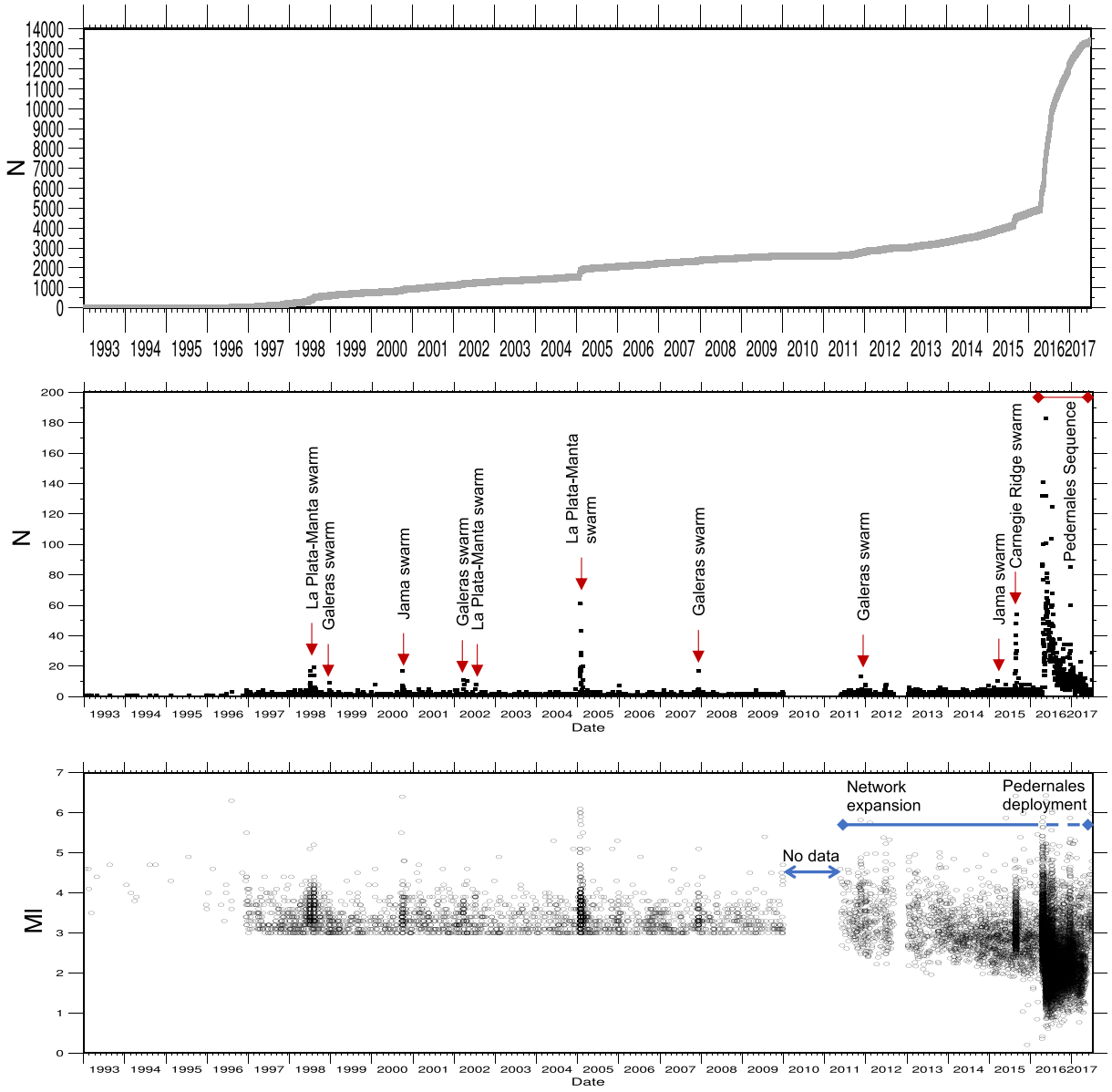


**Figure 15.** (top) Cumulative number of events, (middle) number of events per day, and (bottom) event magnitude per day from 1 January 1993 to 4 July 2017. The horizontal axis is Julian Day. Events through 2009 from Beauval et al. (2013), magnitude cut off of catalog is 3.0. Events from 2011 through 16 April 2016 from IGEPN catalog. No data available for 2010. Events from 17 April 2016 through 4 July 2017 from this study. Noticeable upticks in seismicity above background level (labeled) for the most part reflect earthquake swarms associated with observed slow slip event. Note the decrease in magnitude threshold and increase in number of events detected starting 2011 after upgrade and expansion of IGEPN permanent network and additional decrease in magnitude threshold and increase in number of events detected with temporary deployment for the post Pedernales sequence.

in the upper plate (Figure 7 and Vaca et al., 2018). The location of the composite Galera cluster remains constant during both the interseismic period and in the Pedernales sequence. Seismicity correlates with the northern boundary of maximum aseismic slip (Figure 14), suggesting that a primary control on the location of the composite cluster is structural.

During the Pedernales sequence, spatially focused earthquake clusters migrate in time along the fringes of the afterslip patches and form the composite clusters. Six of the largest magnitude aftershocks in the Pedernales sequence are coincident with the accumulation of afterslip following the mainshock (Figures 9 and 10, and Section 5.3.1 and 5.3.2). These aftershocks locate at the plate interface. The cumulative moment of the six aftershocks and the northern and southern patches of afterslip are equivalent to approximately 23%

of the moment released in the mainshock. Two thirds of this moment come from afterslip; one-third come from the aftershocks.

The Pedernales sequence exhibits a sharp eastward termination in seismicity approximately 90 km from the trench (Figures 5 and 14; Meltzer et al., 2019; Agurto-Detzel et al., 2019). The downdip limit of seismicity occurs where events reach a depth of 30-35 km. This downdip limit is consistent between the catalog and the calibrated relocations. A week after the mainshock an elongated patch of deep afterslip initiated at ~50- to 70-km depth and propagated updip over the following two weeks (Figure 14; Rolandone et al., 2018). The updip limit of deep afterslip coincides with the eastern termination of seismicity in the Pedernales sequence. The region of deep afterslip was also the site of a SSEs in 2015 (Figure 14; Rolandone et al., 2018). These observations suggest a well-defined change in frictional properties marking the transition from the seismogenic zone to the conditionally stable downdip region.

#### 5.4.3. Relationship to Structure-Bathymetry, Topography, Accreted Terranes, and Quaternary Faults

Models of plate coupling and the consistency of earthquake clustering and slip behaviors through multiple seismic cycles suggest structural control on segmentation of the subduction zone offshore northern Ecuador. The seismicity clusters at Manta-Puerto Lopez, Jama, and along the Atacames Seamount chain correlate with seafloor topography on the subducting Carnegie Ridge and Atacames Seamounts. These topographic features have been imaged by active source seismic (Collot et al., 2017; Marcaillou et al., 2016) and appear in residual bathymetry (Bassett & Watts, 2015; Agurto-Detzel et al., 2019.) The composite clusters at Galera and northeast of the Pedernales rupture also correlate with residual bathymetry and gravity anomalies (see Figure 9; Bassett & Watts, 2015), suggesting that focused seismicity in these areas may be controlled by structure and/or deformation (imbricate faults) in the downgoing plate (Angiboust et al., 2014; Menant et al., 2018).

Basement in the forearc is composed of oceanic terranes accreted to the Andean continental margin in the Cretaceous and the Paleocene (Jaillard et al., 2009; Longo & Baldock, 1982). This inherited structure imparts an overall NE-SW structural grain to the forearc (Figure 14f). In the Coastal Range at Manta and Jipijapa, the distribution of seismicity during the Pedernales sequence is similar to what was observed by a dense array of OBS and broadband stations deployed in 2011 to 2013 (Segovia et al., 2018). Earthquakes occur primarily at the plate interface and in the upper part of the subducting plate though some events occur in the upper plate (Figure 7 and Segovia et al., 2018). The eastern termination in seismicity correlates with crustal faults at the edge of the Manabi basin. At this location, the basin lies in contact with basalt of the accreted Piñón Formation. This correlation suggests that the termination in seismicity is due to the rheological contrast between sediments and basalt at depth (Figure 14f and Segovia et al., 2018). This observation is consistent with findings of shear-wave velocity structure from ambient noise tomography and joint inversion of receiver functions and surface-wave dispersion measurements (Koch et al., 2018; Lynner et al., 2020). The region of deep aseismic slip correlates with the Coastal Range at the surface (Figure 14d). Numerical modeling suggests that topographic forearc highs like the Coastal Range coincide with basal accretion of crustal slivers from the subducting oceanic crust (Menant et al., 2018). The formation of crustal duplexes at depth could accompany changes in frictional properties at the downdip end of the coupled portion of the plate interface.

Between Jama and Cojimies, the eastern termination of seismicity coincides approximately with the surface traces of a series of Quaternary faults and lineaments aligned in a NE-SW direction (Figure 14f). These faults are variously named the Quaternary Canaveral faults (Eguez et al., 2003) or the Jama-Quininde faults (Collot et al., 2004; Reyes & Michaud, 2012). While originating in the Paleogene and Neogene (Deniaud, 2000), uplift of the Coastal Range and long profiles of the Jama River indicate these faults are tectonically active (Michaud et al., 2009; Pedoja et al., 2006; Reyes, 2013; Reyes et al., 2018). Farther north, the eastern limit of seismicity correlates with the Mache lineament (Eguez et al., 2003). The clusters of seismicity that trend north toward Atacames follow the eastern edge of the north-south portion of the Borbón basin, where Miocene sediments to the east are uplifted in the Coastal Range (Reyes, 2013; Reyes & Michaud, 2012). The clusters of seismicity at Atacames and Esmeraldas are separated by the Esmeraldas fault. The east-west portion of the coastline from Atacames to Esmeraldas to Rioverde exhibit the highest rates of river incision along the Ecuadorian margin indicating they are uplifting along active structures (Reyes, 2013). While moderate to large earthquakes occur in all the composite clusters, a higher proportion of these events occur north

and east of the mainshock rupture highlighting that the area is tectonically active. As is seen farther south, many of the active structures in the north are associated with the occurrence of the oceanic Piñón Formation or the boundaries between sedimentary basins and uplift of the Coastal Range. This suggests that rheological contrasts at depth between accreted oceanic terranes and sedimentary basins and/or complexity in the downgoing slab play a role in the distribution of slip behavior.

## 6. Conclusions

A dense temporary seismic network deployed in the wake of the 2016 Pedernales Mw 7.8 earthquake provides a detailed view of the evolution of a megathrust rupture postseismic sequence. Composite bands of seismicity made up of more focused individual earthquake clusters containing earthquake swarms and larger magnitude aftershocks occur offshore and along the coast. The composite bands of seismicity are also observed in the interseismic phase and are associated with or border patches of the subduction zone where SSEs occur. The ruptures of Mw > 7.0 earthquake fall within the boundaries of the composite clusters. These earthquake clusters are associated with seafloor topography on the downgoing plate and crustal structure that act as controls on subduction zone segmentation along strike. Deformation adjacent to subducted seamounts triggers seismicity in both the subducting and overlying plate. Onshore structures inherited from terrane accretion remain active as crustal faults that are triggered by megathrust rupture on the plate interface. Many of these structures are associated with the presence of the oceanic Piñón Formation or the boundaries between sedimentary basins and uplift of the coastal ranges. Rheological contrasts between accreted oceanic terranes and sedimentary basins and/or complexity in the downgoing slab play a role in the distribution of slip behavior.

**Acknowledgments**
We used BRTT Antelope software (http://www.brtt.com, last accessed 2017) to generate the automatic catalog. Local seismicity from 1896 through 2009 obtained from Beauval et al. (2013) earthquake catalog; locations from 2011 to April 16, 2016 are from IGEPN online catalog (https://www.igepn.edu.ec/ultimos-sismos; last accessed August 2, 2016). Regional and teleseismic phase arrivals used for HDC relocations were obtained from the International Seismological Centre catalog (http://isc-mirror.iris.washington.edu; last accessed October 2018). Global and regional moment tensors were obtained from gCMT (https://www.globalcmt.org/CMTsearch.html) and NEIC (https://earthquake.usgs.gov/earthquakes/search/; last accessed August 2018). Generic Mapping Tool was used to generate maps and figures (Wessel et al., 2013). Density maps were made using Esri ArcGIS Pro©. Waveform data from the U.S. stations of the Pedernales earthquake aftershock deployment can be obtained from the IRIS Data Management Center, http://www.iris.edu/dms/nodes/dmc/ network code 8G (2016–2017) doi: 10.7914/SN/8G_2016. Data from France and the UK, network code XE, are available through Réseau Sismologique and Géodésique Français (RESIF). The automatic catalog described in this article is included in the supporting information in QuakeML format (https://quake.ethz.ch/quakeml/). This research is supported by NSF EAR Program Awards NSF EAR-1723042 and NSF EAR-1723065. Financial support for the international rapid response effort was provided by U.S. NSF RAPID Program Award EAR-1642498, the Instituto Geofísico at the Escuela Politécnica Nacional (IGEPN) in Quito Ecuador, L'Institut de Recherche pour le Développement (IRD) Géoazur at Université de la Côte d'Azur and Centre d'études et d'expertise sur les risques, l'environnement, la mobilité et l'aménagement (CEREMA) France, and the Natural Environment Research Council (NERC) in the United Kingdom. Soto-Cordero received support from the Marjorie M. Nemes Fellowship, Hispanic Scholarship Fund (HSF) Scholarship, and the U.S. Geological Survey Pathways Program. Agurto-Detzel received support from ANR project ANR-15-CE04-0004 and UCA/JEDI project ANR-15-IDEX-01. We are grateful for stimulating discussions with Jennifer Nealy, Will Yeck, and Harley Benz at the U.S. Geological Survey, National Earthquake Information Center. Any use of trade,

## References

Abe, K. (1979). Size of great earthquakes of 1837–1974 inferred from tsunami data. *Journal of Geophysical Research*, *84*(B4), 1561–1568. https://doi.org/10.1029/JB084iB04p01561

Agurto, H., Rietbrock, A., Ryder, I., & Miller, M. (2012). Seismic-afterslip characterization of the 2010 MW 8.8 Maule, Chile, earthquake based on moment tensor inversion. *Geophysical Research Letters*, *39*, L20303. https://doi.org/10.1029/2012GL053434

Agurto-Detzel, H, Font, Y., Charvis, P., Régnier, M., Rietbrock, A., Ambrois, D., et al. (2019). Ridge subduction and afterslip control aftershock distribution of the 2016 Mw 7.8 Ecuador Earthquake. *Earth and Planetary Science Letters* https://doi.org/10.1016/j.epsl.2019.05.029, *520*, 63, 76

Allen, R. (1982). Automatic phase pickers: Their present use and future prospects. *Bulletin of the Seismological Society of America*, *72*(6B), S225–S242.

Alvarado, A., Audin, L., Nocquet, J. M., Jaillard, E., Mothes, P., Jarrín, P., et al. (2016). Partitioning of oblique convergence in the Northern Andes subduction zone: Migration history and the present-day boundary of the North Andean Sliver in Ecuador. *Tectonics*, *35*, 1048–1065. https://doi.org/10.1002/2016TC004117

Alvarado, A., Ruiz, M., Mothes, P., Yepes, H., Segovia, M., Vaca, M., et al. (2018). Seismic, volcanic, and geodetic networks in Ecuador: Building capacity for monitoring and research. *Seismological Research Letters*, *89*(2A), 432–439. https://doi.org/10.1785/0220170229

Angiboust, S., Glodny, J., Oncken, O., & Chopin, C. (2014). In search of transient subduction interfaces in the Dent Blanche–Sesia Tectonic System (W. Alps). *Lithos*, *205*, 298–321. https://doi.org/10.1016/j.lithos.2014.07.001

Baillard, C., Crawford, W. C., Ballu, V., Hibert, C., & Mangeney, A. (2014). An automatic kurtosis-based *P*- and *S*-phase picker designed for local seismic networks. *Bulletin of the Seismological Society of America*, *104*(1), 394–409. https://doi.org/10.1785/0120120347

Bangs, N. L. B., Gulick, S. P. S., & Shipley, T. H. (2006). Seamount subduction erosion in the Nankai Trough and its potential impact on the seismogenic zone. *Geology*, *34*(8), 701–704. https://doi.org/10.1130/G22451.1

Basset, D., Sandwell, D., Fialko, Y., & Watts, A. B. (2016). Upper-plate controls on co-seismic slip in the 2011 magnitude 9.0 Tohoku-Oki earthquake. *Nature*, *531*(7592), 92–96. https://doi.org/10.1038/nature16945

Bassett, D., & Watts, A. B. (2015). Gravity anomalies, crustal structure, and seismicity at subduction zones: 1. Seafloor roughness and subducting relief. *Geochemistry, Geophysics, Geosystems*, *16*, 1508–1540. https://doi.org/10.1002/2014GC005684

Beauval, C., Yepes, H., Palacios, P., Segovia, M., Alvarado, A., Font, Y., et al. (2013). An earthquake catalog for seismic hazard assessment in Ecuador. *Bulletin of the Seismological Society of America*, *103*(2A), 773–786. https://doi.org/10.1785/0120120270

Beck, S. L., & Ruff, L. J. (1984). The rupture process of the Great 1979 Colombia Earthquake: Evidence for the asperity model. *Journal of Geophysical Research*, *89*(B11), 9281–9291. https://doi.org/10.1029/JB089iB11p09281

Bilek, S. L., & Lay, T. (2018). Subduction zone megathrust earthquakes. *Geosphere*, *14*(4), 1468–1500. https://doi.org/10.1130/GES01608.1

Chlieh, M., Mothes, P. A., Nocquet, J.-M., Jarrin, P., Charvis, P., Cisneros, D., et al. (2014). Distribution of discrete seismic asperities and aseismic slip along the Ecuadorian megathrust. *Earth and Planetary Science Letters*, *400*, 292–301. https://doi.org/10.1016/j.epsl.2014.05.027

Cloos, M. (1992). Thrust-type subduction-zone earthquakes and seamount asperities: A physical model for seismic rupture. *Geology*, *20*(7), 601–604. https://doi.org/10.1130/0091-7613(1992)020<0601:TTSZEA>2.3.CO;2

Collot, J.-Y., Migeon, S., Spence, G., Legonidec, Y., Marcaillou, B., Schneider, J.-L., et al. (2005). Seafloor margin map helps in understanding subduction earthquakes. *Eos, Transactions American Geophysical Union*, *86*(46), 463–465. https://doi.org/10.1029/2005EO460003

Collot, J.-Y., Marcaillou, B., Sage, F., Michaud, F., Agudelo, W., Charvis, P., et al. (2004). Are rupture zone limits of great subduction earthquakes controlled by upper plate structures? Evidence from multichannel seismic reflection data acquired across the northern Ecuador–southwest Colombia margin. *Journal of Geophysical Research*, *109*, B11103. https://doi.org/10.1029/2004JB003060

firm, or product names is for descriptive purposes only and does not imply endorsement by the U.S. Government. We thank the Associate Editor and anonymous reviewers for their thorough review and helpful comments to improve the manuscript.

Collot, J.-Y., Sanclemente, E., Nocquet, J.-M., Leprêtre, A., Ribodetti, A., Jarrin, P., et al. (2017). Subducted oceanic relief locks the shallow megathrust in central Ecuador. *Journal of Geophysical Research: Solid Earth*, *122*, 3286–3305. https://doi.org/10.1002/2016JB013849

Croux, C., & Rousseeuw, P. J. (1992). Time-Efficient Algorithms for Two Highly Robust Estimators of Scale. In *Computational Statistics*, (pp. 411–428). Heidelberg: Physika-Verlag. https://doi.org/10.1007/978-3-662-26811-7_58

Das, S., & Watts, A. B. (2009). Effect of subducting seafloor topography on the rupture characteristics of great subduction zone earthquakes. In S. Lallemand, & F. Funiciello (Eds.), *Subduction Zone Geodynamics*, (pp. 103–118). Berlin Heidelberg: Springer.

Deniaud, Y. (2000). *Enregistrement sédimentaire et structural de l'évolution géodynamique des Andes Equatoriennes au cours du Néogène: étude des bassins d'avant-arc et bilan de masse*. (PhD Thesis). Université Joseph Fourier, Grenoble, France.

Eguez, A., Alvarado, A., Yepes, H., Machette, M. N., Costa, C., & Dart, R. L. (2003). Database and Map of Quaternary faults and folds of Ecuador and its offshore regions. USGS. Retrieved from http://pubs.usgs.gov/of/2003/ofr-03-289/

Font, Y., Segovia, M., Vaca, S., & Theunissen, T. (2013). Seismicity patterns along the Ecuadorian subduction zone: New constraints from earthquake location in a 3-D a priori velocity model. *Geophysical Journal International*, *193*(1), 263–286. https://doi.org/10.1093/gji/ggs083

Gomberg, J., & Sherrod, B. (2014). Crustal earthquake triggering by modern great earthquakes on subduction zone thrusts. *Journal of Geophysical Research: Solid Earth*, *119*, 1235–1250. https://doi.org/10.1002/2012JB009826

Graindorge, D., Calahorrano, A., Charvis, P., Collot, J.-Y., & Bethoux, N. (2004). Deep structures of the Ecuador convergent margin and the Carnegie Ridge, possible consequence on great earthquakes recurrence interval. *Geophysical Research Letters*, *31*, L04603. https://doi.org/10.1029/2003GL018803

Gutscher, M.-A., Malavieille, J., Lallemand, S., & Collot, J.-Y. (1999). Tectonic segmentation of the North Andean margin: Impact of the Carnegie Ridge collision. *Earth and Planetary Science Letters*, *168*(3), 255–270. https://doi.org/10.1016/S0012-821X(99)00060-6

Hanks, T. C., & Kanamori, H. (1979). A moment magnitude scale. *Journal of Geophysical Research*, *84*(B5), 2348–2350. https://doi.org/10.1029/JB084iB05p02348

Hayes, G. P., Bergman, E., Johnson, K. L., Benz, H. M., Brown, L., & Meltzer, A. S. (2013). Seismotectonic framework of the 2010 February 27 Mw 8.8 Maule, Chile earthquake sequence. *Geophysical Journal International*, *195*(2), 1034–1051. https://doi.org/10.1093/gji/ggt238

Hayes, G. P., Moore, G. L., Portner, D. E., Hearne, M., Flamme, H., Furtney, M., & Smoczyk, G. M. (2018). Slab2, a comprehensive subduction zone geometry model. *Science*, *362*(6410), 58–61. https://doi.org/10.1126/science.aat4723

Hicks, S. P., Rietbrock, A., Ryder, I. M. A., Lee, C.-S., & Miller, M. (2014). Anatomy of a megathrust: The 2010 M8.8 Maule, Chile earthquake rupture zone imaged using seismic tomography. *Earth and Planetary Science Letters*, *405*, 142–155. https://doi.org/10.1016/j.epsl.2014.08.028

Holtkamp, S. G., & Brudzinski, M. R. (2011). Earthquake swarms in circum-Pacific subduction zones. *Earth and Planetary Science Letters*, *305*(1-2), 215–225. https://doi.org/10.1016/j.epsl.2011.03.004

Holtkamp, S. G., Pritchard, M. E., & Lohman, R. B. (2011). Earthquake swarms in South America. *Geophysical Journal International*, *187*(1), 128–146. https://doi.org/10.1111/j.1365-246X.2011.05137.x

Hoskins, M., Meltzer, A., Soto-Cordero, L., J. Stachnik, Beck, S. L., Lynner, C., ... Rietbrock, A. (2018). Variable slip modes in postseismic deformation North of the April 16, 2016 Mw 7.8 Pedernales, Ecuador megathrust earthquake. Fall Meeting, AGU, Washington, DC, 10-14 Dec. Published Online 2019 https://doi.org/10.1002/essoar.10500871.1

Hoskins, M., Meltzer, A., Stachnik, J. C., Agurto-Detzel, H., Alvarado, A., Beck, S., ... Ruiz, M. (2019). Structural controls on postseismic deformation following the Mw 7.8 Pedernales, Ecuador megathrust earthquake: Insights from joint tomographic inversion and aftershock relocation. Fall Meeting, AGU, San Francisco, CA, 9-13 Dec.

Husen, S., Kissling, E., & Quintero, R. (2002). Tomographic evidence for a subducted seamount beneath the Gulf of Nicoya, Costa Rica: The cause of the 1990 Mw = 7.0 Gulf of Nicoya earthquake. *Geophysical Research Letters*, *29*(8), 1238. https://doi.org/10.1029/2001GL014045

International Seismological Centre. (2016). On-line Bulletin. *Internatl. Seismol. Cent., Thatcham, United Kingdom*. https://doi.org/10.31905/D808B830

Jaillard, É., Hérail, G., Monfret, T., Díaz-Martínez, E., Baby, P., Lavenu, A., & Dumont, J. F. (2000). Tectonic evolution of the Andes of Ecuador, Peru, Bolivia and northernmost Chile. *Tectonic Evolution of South America*, *31*, 481–559.

Jaillard, E., Lapierre, H., Ordoñez, M., Álava, J. T., Amórtegui, A., & Vanmelle, J. (2009). Accreted oceanic terranes in Ecuador: Southern edge of the Caribbean Plate? *Geological Society, London, Special Publications*, *328*(1), 469–485. https://doi.org/10.1144/SP328.19

Jordan, T. H., & Sverdrup, K. A. (1981). Teleseismic location techniques and their application to earthquake clusters in the South-Central Pacific. *Bulletin of the Seismological Society of America*, *71*(4), 1105–1130.

Kanamori, H., & McNally, K. C. (1982). Variable rupture mode of the subduction zone along the Ecuador-Colombia coast. *Bulletin of the Seismological Society of America*, *72*(4), 1241–1253.

Karasözen, E., Nissen, E., Bergman, E. A., Johnson, K. L., & Walters, R. J. (2016). Normal faulting in the Simav graben of western Turkey reassessed with calibrated earthquake relocations. *Journal of Geophysical Research: Solid Earth*, *121*, 4553–4574. https://doi.org/10.1002/2016JB012828

Kelleher, J. A. (1972). Rupture zones of large South American earthquakes and some predictions. *Journal of Geophysical Research*, *77*(11), 2087–2103. https://doi.org/10.1029/JB077i011p02087

Kendrick, E., Bevis, M., Smalley, R., Brooks, B., Vargas, R. B., Lauíra, E., & Fortes, L. P. S. (2003). The Nazca–South America Euler vector and its rate of change. *Journal of South American Earth Sciences*, *16*(2), 125–131. https://doi.org/10.1016/S0895-9811(03)00028-2

Kennett, B. L. N., & Engdahl, E. R. (1991). Traveltimes for global earthquake location and phase identification. *Geophysical Journal International*, *105*(2), 429–465. https://doi.org/10.1111/j.1365-246X.1991.tb06724.x

Kennett, B. L. N., Engdahl, E. R., & Buland, R. (1995). Constraints on seismic velocities in the Earth from traveltimes. *Geophysical Journal International*, *122*(1), 108–124. https://doi.org/10.1111/j.1365-246X.1995.tb03540.x

Koch, C., Lynner, C., Delph, J., Beck, S., Meltzer, A., Hoskins, M., ... Regnier, M. M. (2018). Crustal structure of the Ecuadorian Forearc, from the Joint Inversion of Receiver Functions and Ambient Noise Dispersion Data, T43E-0459, Fall Meeting, AGU, Washington D.C. 10-14 Dec.

Kodaira, S., Takahashi, N., Nakanishi, A., Miura, S., & Kaneda, Y. (2000). Subducted seamount imaged in the rupture zone of the 1946 Nankaido earthquake. *Science*, *289*(5476), 104–106. https://doi.org/10.1126/science.289.5476.104

León-Ríos, S., Agurto-Detzel, H., Rietbrock, A., Alvarado, A., Beck, S., Charvis, P., et al. (2019). 1D-velocity structure and seismotectonics of the Ecuadorian margin inferred from the 2016 Mw7.8 Pedernales aftershock sequence. *Tectonophysics*, *767*, 228165. https://doi.org/10.1016/j.tecto.2019.228165

Lomax, A., Satriano, C., & Vassallo, M. (2012). Automatic picker developments and optimization: FilterPicker—A robust, broadband picker for real-time seismic monitoring and earthquake early warning. *Seismological Research Letters*, *83*(3), 531–540. https://doi.org/10.1785/gssrl.83.3.531

Longo, R, & Baldock, J. (1982). National geologic map of the Republic of Ecuador. Dirección General de Geológia y Minas (DGGM).

Lonsdale, P. (1978). Near-bottom reconnaissance of a fast-slipping transform fault zone at the Pacific-Nazca Plate boundary. *The Journal of Geology*, *86*(4), 451–472. https://doi.org/10.1086/649712

Lynner, C., Koch, C., Beck, S., Meltzer, A., Soto-Cordero, L., Hoskins, M., et al. (2020). Upper-plate structure in Ecuador coincident with the subduction of the Carnegie Ridge and the southern extent of large mega-thrust earthquakes. *Geophysical Journal International*, *220* (3), 1965–1977. https://doi.org/10.1093/gji/ggz558

Marcaillou, B., & Collot, J.-Y. (2008). Chronostratigraphy and tectonic deformation of the North Ecuadorian–South Colombian offshore Manglares forearc basin. *Marine Geology*, *255*(1), 30–44. https://doi.org/10.1016/j.margeo.2008.07.003

Marcaillou, B., Collot, J.-Y., Ribodetti, A., d'Acremont, E., Mahamat, A.-A., & Alvarado, A. (2016). Seamount subduction at the North-Ecuadorian convergent margin: Effects on structures, inter-seismic coupling and seismogenesis. *Earth and Planetary Science Letters*, *433*, 146–158. https://doi.org/10.1016/j.epsl.2015.10.043

McNamara, D. E., Benz, H. M., Herrmann, R. B., Bergman, E. A., Earle, P., Meltzer, A., et al. (2014). The Mw 5.8 Mineral, Virginia, earthquake of August 2011 and aftershock sequence: Constraints on earthquake source parameters and fault geometry. *Bulletin of the Seismological Society of America*, *104*(1), 40–54. https://doi.org/10.1785/0120130058

Meltzer, A., Beck, S., Ruiz, M., Hoskins, M., Soto-Cordero, L., Stachnik, J. C., et al. (2019). The 2016 Mw 7.8 Pedernales Earthquake, Ecuador: RAPID Response Deployment. *Seismological Research Letters*, *90*(3), 1346–1354. https://doi.org/10.1785/0220180364

Menant, A., Angiboust, S., Gerya, T., Lacassin, R., Simoes, M., & Grandin, R. (2018). Towards an integrated vision of tectonic underplating and associated deformation in subduction zones, insights from high-resolution numerical modeling. *20th EGU General Assembly, EGU2018, Proceedings from the Conference Held 4-13 April, 2018 in Vienna, Austria*, 7585.

Mendoza, C., & Dewey, J. W. (1984). Seismicity associated with the great Colombia-Ecuador earthquakes of 1942, 1958, and 1979: Implications for barrier models of earthquake rupture. *Bulletin of the Seismological Society of America*, *74*(2), 577–593.

Michaud, F., Witt, C., & Royer, J.-Y. (2009). Influence of the subduction of the Carnegie volcanic ridge on Ecuadorian geology: Reality and fiction. In S. M. Kay, V. A. Ramos, & W. R. Dickinson (Eds.), *Backbone of the Americas: Shallow subduction, plateau uplift, and ridge and terrane collision* (pp. 217–228). Washington DC: Geological Society of America. https://doi.org/10.1130/2009.1204(10)

Mothes, P. A., Nocquet, J.-M., & Jarrín, P. (2013). Continuous GPS network operating throughout Ecuador. *Eos, Transactions American Geophysical Union*, *94*(26), 229–231. https://doi.org/10.1002/2013EO260002

Nealy, J. L., Benz, H. M., Hayes, G. P., Bergman, E. A., & Barnhart, W. D. (2017). The 2008 Wells, Nevada, network operating throughout: Source constraints using calibrated multiple-event relocation and InSAR. *Bulletin of the Seismological Society of America*, *107*(3), 1107–1117. https://doi.org/10.1785/0120160298

NEIC. (2016a). M 6.7-33km SE of Muisne, Ecuador—Event page. Retrieved from https://earthquake.usgs.gov/earthquakes/eventpage/us10005i5t/executive

NEIC. (2016b). M 6.9-24km NW of Rosa Zarate, Ecuador - Event Page. Retrieved from https://earthquake.usgs.gov/earthquakes/eventpage/us10005i9n/executive

NEIC. (2016c). M 7.8 Muisne, Ecuador - Event Page. Retrieved from https://earthquake.usgs.gov/earthquakes/eventpage/us20005j32/executive

NEIC. (2017). Earthquake catalog search: https://earthquake.usgs.gov/earthquakes/search/, last accessed December 2018.

Nocquet, J.-M., Jarrin, P., Vallée, M., Mothes, P. A., Grandin, R., Rolandone, F., et al. (2017). Supercycle at the Ecuadorian subduction zone revealed after the 2016 Pedernales earthquake. *Nature Geoscience*, *10*(2), 145–149. https://doi.org/10.1038/ngeo2864

Nocquet, J.-M., Villegas-Lanza, J. C., Chlieh, M., Mothes, P. A., Rolandone, F., Jarrin, P., et al. (2014). Motion of continental slivers and creeping subduction in the northern Andes. *Nature Geoscience*, *7*(4), 287–291. https://doi.org/10.1038/ngeo2099

Pavlis, G. L., Vernon, F., Harvey, D., & Quinlan, D. (2004). The generalized earthquake-location (GENLOC) package: An earthquake-location library. *Computers & Geosciences*, *30*(9-10), 1079–1091. https://doi.org/10.1016/j.cageo.2004.06.010

Pedoja, K., Dumont, J. F., Lamothe, M., Ortlieb, L., Collot, J.-Y., Ghaleb, B., et al. (2006). Plio-Quaternary uplift of the Manta Peninsula and La Plata Island and the subduction of the Carnegie Ridge, central coast of Ecuador. *Journal of South American Earth Sciences*, *22*(1-2), 1–21. https://doi.org/10.1016/j.jsames.2006.08.003

Peng, Z., & Gomberg, J. (2010). An integrated perspective of the continuum between earthquakes and slow-slip phenomena. *Nature Geoscience*, *3*(9), 599–607. https://doi.org/10.1038/ngeo940

Reyes, P. (2013). *Evolution du relief le long des marges actives: étude de la déformation Plio-Quaternaire de la cordillère côtière d'Equateur* (PhD Thesis). Université Nice Sophia Antipolis.

Reyes, P., & Michaud, F. (2012). *Mapa Geologico de la Margen Costera Ecuatoriana*. Quito, Ecuador: EP PetroEcuador - IRD.

Reyes, P. S. B., Valarezo, M. E., Córdova, J., Michaud, F. A., & Zapata, C. (2018). Quantitative morphometric analysis of the Jama River profile in a tectonically active margin (Northwestern Ecuador). *Journal of Mountain Science*, *15*(5), 966–975. https://doi.org/10.1007/s11629-017-4751-y

Reynaud, C., Jaillard, É., Lapierre, H., Mamberti, M., & Mascle, G. H. (1999). Oceanic plateau and island arcs of southwestern Ecuador: Their place in the geodynamic evolution of northwestern South America. *Tectonophysics*, *307*(3), 235–254. https://doi.org/10.1016/S0040-1951(99)00099-2

Rolandone, F., Nocquet, J.-M., Mothes, P. A., Jarrin, P., Vallée, M., Cubas, N., et al. (2018). Areas prone to slow slip events impede earthquake rupture propagation and promote afterslip. *Science Advances*, *4*(1), eaao6596. https://doi.org/10.1126/sciadv.aao6596

Scholz, C. H., & Small, C. (1997). The effect of seamount subduction on seismic coupling. *Geology*, *25*(6), 487–490. https://doi.org/10.1130/0091-7613(1997)025<0487:TEOSSO>2.3.CO;2

Segovia, M., Font, Y., Régnier, M., Charvis, P., Galve, A., Nocquet, J.-M., et al. (2018). Seismicity distribution near a subducting seamount in the Central Ecuadorian subduction zone, space-time relation to a slow-slip event. *Tectonics*, *37*(7), 2106–2123. https://doi.org/10.1029/2017TC004771

Soto-Cordero, L. (2019). *Earthquake and tectonic processes in the Mid-Atlantic US Passive Margin and the Ecuador Subduction Zone* (Doctoral). Lehigh University, Bethlehem, PA, United States (USA).

Swenson, J. L., & Beck, S. L. (1996). Historical 1942 Ecuador and 1942 Peru subduction earthquakes and earthquake cycles along Colombia-Ecuador and Peru subduction segments. *Pure and Applied Geophysics*, *146*(1), 67–101. https://doi.org/10.1007/BF00876670

Vaca, S., Vallée, M., Nocquet, J.-M., Battaglia, J., & Régnier, M. (2018). Recurrent slow slip events as a barrier to the northward rupture propagation of the 2016 Pedernales earthquake (Central Ecuador). *Tectonophysics*, *724–725*, 80–92. https://doi.org/10.1016/j.tecto.2017.12.012

Vallée, M., Nocquet, J.-M., Battaglia, J., Font, Y., Segovia, M., Régnier, M., et al. (2013). Intense interface seismicity triggered by a shallow slow slip event in the Central Ecuador subduction zone. *Journal of Geophysical Research: Solid Earth*, *118*, 2965–2981. https://doi.org/10.1002/jgrb.50216

Wang, K., & Bilek, S. L. (2011). Do subducting seamounts generate or stop large earthquakes? *Geology*, *39*(9), 819–822. https://doi.org/10.1130/G31856.1

Wang, K., & Bilek, S. L. (2014). Invited review paper: Fault creep caused by subduction of rough seafloor relief. *Tectonophysics*, *610*, 1–24. https://doi.org/10.1016/j.tecto.2013.11.024

Wessel, P., Smith, W. H. F., Scharroo, R., Luis, J., & Wobbe, F. (2013). Generic Mapping Tools: Improved version released, Eos Trans. *AGU*, *94*(45), 409–410. https://doi.org/10.1002/2013EO450001

Wetzler, N., Lay, T., Brodsky, E. E., & Kanamori, H. (2018). Systematic deficiency of aftershocks in areas of high coseismic slip for large subduction zone earthquakes. *Science Advances*, *4*(2), eaao3225. https://doi.org/10.1126/sciadv.aao3225

White, S. M., Trenkamp, R., & Kellogg, J. N. (2003). Recent crustal deformation and the earthquake cycle along the Ecuador–Colombia subduction zone. *Earth and Planetary Science Letters*, *216*(3), 231–242. https://doi.org/10.1016/S0012-821X(03)00535-1

Ye, L., Kanamori, H., Avouac, J.-P., Li, L., Cheung, K. F., & Lay, T. (2016). The 16 April 2016, MW7.8 (MS7.5) Ecuador earthquake: A quasi-repeat of the 1942 MS7.5 earthquake and partial re-rupture of the 1906 MS8.6 Colombia–Ecuador earthquake. *Earth and Planetary Science Letters*, *454*, 248–258. https://doi.org/10.1016/j.epsl.2016.09.006

Yeck, W. L., Patton, J. M., Johnson, C. E., Kragness, D., Benz, H. M., Earle, P. S., et al. (2019). GLASS3: A standalone multiscale seismic detection associator. *Bulletin of the Seismological Society of America*, *109*(4), 1469–1478. https://doi.org/10.1785/0120180308

Yepes, H., Audin, L., Alvarado, A., Beauval, C., Aguilar, J., Font, Y., & Cotton, F. (2016). A new view for the geodynamics of Ecuador: Implication in seismogenic source definition and seismic hazard assessment. *Tectonics*, *35*, 1249–1279. https://doi.org/10.1002/2015TC003941

Yi, L., Xu, C., Wen, Y., Zhang, X., & Jiang, G. (2018). Rupture process of the 2016 Mw 7.8 Ecuador earthquake from joint inversion of InSAR data and teleseismic P waveforms. *Tectonophysics*, *722*, 163–174. https://doi.org/10.1016/j.tecto.2017.10.028

Yoshimoto, M., Kumagai, H., Acero, W., Ponce, G., Vásconez, F., Arrais, S., et al. (2017). Depth-dependent rupture mode along the Ecuador-Colombia subduction zone. *Geophysical Research Letters*, *44*, 2203–2210. https://doi.org/10.1002/2016GL071929